A NOVEL POSITIONAL SENSOR FOR 3D VASCULAR RECONSTRUCTION

by

John Henry Merritt

A dissertation submitted to the faculty of
The University of North Carolina at Charlotte
in partial fulfillment of the requirements
for the degree of Doctor of Philosophy in
Information Technology

Charlotte

2011

Approved by:

____
Dr. M. Taghi Mostafavi

____
Dr. Mohammad R. Sayeh

____
Dr. Kalpathi R. Subramanian

____
Dr. Mirsad Hadzikadic

____
Dr. S. Mehdi Miri

____
Dr. Susan M. Sell

ABSTRACT

JOHN HENRY MERRITT. A novel positional sensor for 3D vascular reconstruction. (Under the direction of DR. M. TAGHI MOSTAFAVI)

Intravascular ultrasound (IVUS) is a device that is surgically inserted into a femoral artery, or vein, to aid in the diagnosis of cardiovascular disease. Correctly locating the IVUS tip facilitates accurate 3D vascular reconstruction. Researchers are actively investigating different methods, such as: stereo X-rays, radio triangulation, computer-aided tomography (CAT) scans, etc., to produce quality 3D graphical vascular images. Each of these methods has their pros and cons, however they all require external sensors and some are bulky and complicated to operate.

This research investigates an accelerometer, constructed from a multi-mode fiber-optic cable, and studies its performance with multi-mode fiber interferometry technology (speckle-gram analysis) and presents experimental evidence to support its suitability for tracking an IVUS sensor in vivo, leading to real-time 3D reconstruction of internal arterial segments. The system resulting from this study is expected to be simple, small, and economically feasible, to bridge the diagnostic/treatment time gap and eliminate the need for external tracking equipment. Non-linear models and analysis of variance methodologies are presented to verify that the fiber-optic accelerometer is functioning within experimental error which can provide accurate spatial tracking. The results from this study show that the fiber accelerometer is performing as well as a micro-electromechanical machine system (MEMS) accelerometer and, unlike the MEMS, it is immune to environmental noise. The potential system is expected to reduce the computation necessary to perform 3D vascular reconstruction from IVUS data, leading to improvements in, and the reduction of, the diagnostic/treatment time-line. Also, the performance and sensitivity of this novel positional sensor is expected to improve with appropriate changes in the craftsmanship of the fiber accelerometer and testing apparatus.

DEDICATION

This dissertation is dedicated to my lovely wife Nichol Marie and our three boys: Benjamin Henry, John Paul and Maxwell James. Without their loving support and patience, this may not have been.

ACKNOWLEDGMENTS

I am grateful to my thesis advisor Dr. M. Taghi Mostafavi for seeing my potential and challenging me to investigate a technology that heretofore was not considered. And, to Dr. Mohammad Sayeh for his instruction on the basics of fiber interferometry and the associated laboratory experimentation. And, to my dissertation committee members: Dr. Kalpathi R. Subramanian, Dr. Mirsad Hadzikadic, Dr. S. Mehdi Miri for their support and feedback. And, to Dr. Susan M. Sell for imparting fairness and ensuring that I met all deadlines and requirements for graduation.

Of course, I remember those who knew of my doctorate journey, but are no longer with us: my father Clarence Wallace Harry Merritt, my grandmother Thelma Amelia Merritt and my mother-in-law Mary Virgina Bakalar.

TABLE OF CONTENTS

LIST OF TABLES

LIST OF FIGURES

CHAPTER 1: INTRODUCTION

Intravascular ultrasound (IVUS) is a sensor and processing system that is used to examine the internal structure of arteries or veins at any location large enough for the catheter.[1] The IVUS is a device that is surgically inserted into a femoral artery and threaded up to the heart and is a popular means for examining the interior of the artery, aiding physicians in the diagnosis of cardiovascular disease. The IVUS can detect plaques, embolisms, constrictions, etc. but it is not yet an indispensable tool for such diagnosis [1, 2].

The IVUS is a rapidly spinning ultrasound transmitter and receiver of soundings, or echos, and is capable of producing images of the soft tissue within the artery, at any given point. Collecting IVUS data while it is in motion results in a series of cross-sectional images, see figure 1.1. Researchers are actively investigating various methods to transform the IVUS image sets into a spatially accurate 3D vascular reconstruction, yet the goal of an all-in-one real-time 3D IVUS device remains elusive. The process of creating 3D vascular reconstruction is time consuming and requires human intervention[3, 4, 5]. What is needed is a device to locate the 3D positional coordinates of the planar 2D IVUS cross-sectional images, in order to reduce the mathematical complexity and computer processing time, and enable the real-time reconstruction for 3D computer visualization of the vascular segment. Consequently, it has the potential to reduce the time between the IVUS procedure, for diagnostics, and treatment – thus, prevent the need for follow-up surgeries.

[1] For simplicity, we will refer to any one of those locations as arterial, since the primary use for IVUS catheters is in the examination of arterial structures.

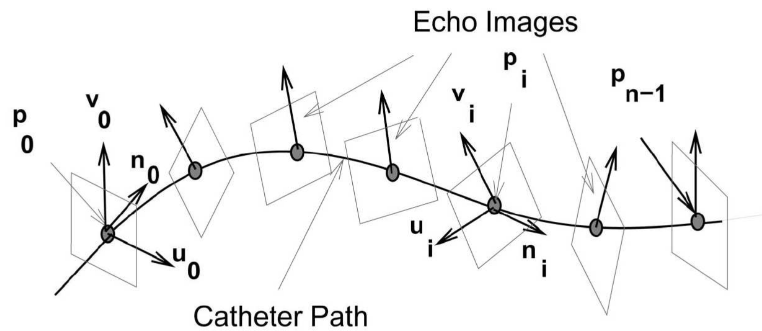

Figure 1.1: Tracking the IVUS sensor requires the determination of 3D coordinates, p_i, and the normal to the cross-section, n_i. The sensor rotation is obtained from v_i or u_i. External sensors, such as X-rays, are used along with a suite of analysis software to compute the 3D points.

1.1 Significance

Currently, 3D IVUS vascular mapping systems are confined to research laboratories, but, based on the abundance of literature in this field, this research is very active. There are several issues with IVUS that prevent universal acceptance: one being the difficulty of generating real-time 3D arterial views. A real-time arterial reconstruction that shows the internal view of the artery, would give the physician the opportunity to readily diagnose and treat patients with minimal invasion, in rapid time and with improved accuracy; all of which contributes to improved patient experiences which may lead to reduced recovery times and minimize complications.

Major cardiovascular diseases are the number one killer of people in the United States, accounting for over 820,000 deaths in 2006 and 616,067 deaths in 2007[6, 7]. Of those in 2006, for instance, over 650,000 deaths were categorized as diseases of the heart and circulatory system. These numbers are coming down due to several factors. One important factor, in reducing this death rate, is improved diagnostics. Such improvements allow the practitioner to reduce treatment turnaround times and reduce the guess work associated with interpreting a less than ideal presentations of the patients' vitals and physical anomalies. During the past few decades, intravascular ultrasound (IVUS) has provided improvements to the views of the interior structure and composition of coronary arterial system. As such, the IVUS is the primary tool used to directly observe arterial plaques[8].

Over the lifetime of IVUS, incremental advances on the data presentation have been made. Computer software is able to automatically highlight a number of features. Substantial software analysis, often requiring human intervention, is needed to accurately reconstruct the 3D curved structure of the artery[9, 10, 3]. Kirbas provides a comprehensive summary of software techniques actively being researched, that perform the reconstruction using software [11], see section 2.1.1.1. 3D arterial reconstruction is very active research topic; and not completely solved. Software solutions are not a stop-gap and require a great deal of computation and "hand" manipulation to identify corresponding feature points, to guide the reconstruction. Data fusion of multiple technologies is able to generate accurate 3D reconstructions but require data from large and expensive CAT or MRI systems. Cardiop-B® is the first commercially available 3D cardiovascular imaging system using multiple angiographic views and can perform the 3D reconstruction in real-time[12], however it is unable to image the interior structure of the artery. Some IVUS systems are able to reproduce 3D structural representations, however, they require human assistance to identify corresponding points [13, 14].

The recent S.T.L.L.R. study[2], sponsored by Johnson & Johnson, showed that current stent deployment techniques led to some form of geographic miss in 66.5% of patients. Misplacement rates that high, lead to a significant recurrence of problems, and may lead to additional complications. The study concluded that "a re-examination of stent placement technique including the use of IVUS is certainly warranted." [1]

The modus operandi for operating an IVUS system is that the clinician mentally constructs the 3D representation from a video of the 2D cross-section images. In particular, when using cardiovascular catheters, the display is a poor quality monochro-

[2] S.T.L.L.R. stands for "The Impact of Stent Deployment Techniques on Clinical Outcomes on Patients Treated with the Cypher(R) Stent."

matic 2D X-ray fluoroscope. Considerable training and practice is required to determine the structures visible in 2D ultrasounds. Diagnostic analysis is done on a qualitative basis requiring days, weeks or even months; many times the patient must return for painful, followup catheter procedures.

1.2 Research Question

The literature survey suggests that a more accurate computer rendering of a patents vascular segments may lead to a more accurate medical diagnosis and treatment plan. The time-gap from data collection to diagnosis and treatment is very real and lengthy enough that treatment does not occur during the initial exploratory procedure. An IVUS catherization is risky and arterial puncture is a major concern. The research literature suggests that shortening that diagnostic/treatment time-line would be beneficial to the patient in terms of cost, physical discomfort and recovery.

The novel positional sensor, herein investigated, has the potential to simplify the process of generating 3D vascular views from the 2D IVUS data, by providing the 3D coordinates of the IVUS sensor at the catheter tip, leading to the reduction of the diagnostic/treatment time-line; quite possibly eliminating it. This new positional senor emits no harmful radiation and does not require any external tracking devices, eliminating bulk and complexity; because, it is a fiber optic cable that uses light. A positional sensor constructed from a fiber optic cable will result is a smaller, cheaper and safer device which should simplify the mathematics required to transform 2D IVUS images into a 3D vascular reconstruction. The lack of literature on IVUS or catheter tracking systems suggest that they are not commonly available – for any number of reasons – forcing doctors to rely systems that merely present the 2D images without the possibility of rendering them in 3D.

Because the diameter of a fiber cable is very small it is a natural fit for tracking the tip of a cardiovascular catheter in vivo. It is important that the device not introduce additional physical bulk so as to restrict the locations that the catheter can navigate;

a thin fiber cable – thinner than a human hair – meets that requirement.

This research presents an architectural design of a fiber positional sensor – more precisely, a fiber accelerometer – and a set of four experiments, using a prototype of the device, to illustrate its potential performance. In brief, the experimentation shows that the fiber accelerometer measurements are indistinguishable from a micro-electromechanical system (MEMS) accelerometer of an iPod®[3]. Additionally, the fiber accelerometer is not subject to electromagnetic noise; the iPod® accelerometer is. With proper manufacturing, the fiber accelerometer has the potential to be extremely sensitive and accurate sensor. It is natural to infer, from this research, that this device could have an enormous impact in the IVUS diagnostic community; leading to exciting expectations for diagnostics and treatment of cardiovascular disease.

1.3 Organization of this document

Chapter 2 discusses the related literature as applicable to the field of 3D cardiovascular reconstruction or vascular mapping. The discussion briefly mentions hardware in a general context for data collection, then presents a general list of software techniques for the analysis and 3D reconstruction. This chapter presents a discussion of the IVUS system and other hardware devices used to collect the vascular data. It concludes with a brief discussion of the pros and cons of the current hardware technology used for vascular diagnostics and 3D reconstruction. Section 2.2 provides a brief introduction into the field of fiber optics; but, only those technologies that relate to this dissertation; specifically, interferometers that are suitable for motion or stress sensing. Fiber Bragg's grating (FBG) sensors are very well suited for a catheter tip tracking device, however, special fiber construction techniques are required to produce it.

Chapter 3 begins the presentation of a "novel positional sensor for 3D vascular reconstruction." It presents the experimental design and methodology.

[3]iPod is a registered trademark of Apple Inc.

Chapter 4 describes the experimental setups in detail and presents the results.

Chapter 5 summarizes the experimental results and discusses potential and future research.

Appendix A presents six possible interferometer laboratory and product schematics.

Appendix B presents the statistical analysis equations.

Appendix C presents the physics of a pendulum.

CHAPTER 2: BACKGROUND LITERATURE

This review discusses the on-going research in vascular reconstruction; from both a hardware and software perspective. These technologies range from those in the early experimental stages to commercially available and clinically operational systems. This section will illustrate that many of these systems are large, expensive and produce harmful radiation. The novel position sensor developed in this dissertation research addresses these issues to provide a smaller, cheaper and safer device to perform a necessary function for 3-D vascular reconstruction. If possible, this new position sensor may replace the systems that emit harmful radiation.

The are two sections to this literature review. The first section discusses the medically applicable software and hardware that directly relates to 3-D vascular reconstruction. The devices that collect the data, generally, do so by emitting harmful radiation (X-rays, fluoroscopy, angiography, CAT, etc) and produce digital video or image sequences. Elaborate software techniques are generally tightly coupled with the hardware, but many research areas focus on software-only image analysis. These software-only systems eventually make their way back to the hardware allowing for a more detailed real-time analysis.

The second section presents a selection of literature in the field of fiber optics; more specifically, the field of interferometry – the study of interference patterns of light. This material is directly related to the new sensor presented in this dissertation. The new sensor is a fiber optic cable and the analysis of the light patterns within the fiber are the central focus of this research.

Another section, which is not part of the literature review, briefly illustrates the MEMS accelerometer used for validating the experimental results.

2.1 Vascular reconstruction

Vascular reconstruction is the application domain for the "novel positional sensor for 3D vascular reconstruction." Final validation of the positional sensor will come from clinical analysis using traditional catheter tracking technologies.

The general trend for analyzing medical imagery – video and/or images – is to apply numerous processing filters on the images in order to reduce noise, determine edges, segment them, all in an effort to find continuity and determine if they comprise interesting features or salient objects. The data collected are not done so under ideal conditions and there is the never-ending battle with noise; from patient movement, sensor noise, sensor movement, image processing artifacts, etc. Current hardware and software must continually be calibrated to ensure the best possible data capture.

2.1.1 Vascular mapping

Vascular tree reconstruction and intravascular studies usually involves the collection and analysis of medical imagery. The imagery is usually in the form of still images or video. From an image processing perspective, the two types are quite similar. They are a sequence of low resolution gray scale images, usually recorded from analog devices and converted to digital and stored. For video, a temporal context is available from which to extract salient information. Considerable research in the field of computer vision has attempted to mimic biological vision systems, especially for motion detection and tracking.

Vascular mapping or vascular segmentation is nicely summarized by Kirbas and Quek [11], wherein they conclude that researchers are actively searching for improvements to new and existing hardware and software systems, to accurately display the reconstructed vascular tree. The data collection hardware: CAT, micro-CT, MRI, X-Ray, etc., suffer from resolution and noise issues and the algorithms suffer from errors and speed. CardiOp-B® can construct the 3-D vascular tree representation from two or more angiography images [12].

The following presents a summary of vascular mapping techniques, ranging from those mentioned in Kirbas et al. [11] to early fiber shape sensor research. While many of the techniques mentioned are meant to solve the vascular reconstruction, the techniques presented are applicable to tracking and signal processing in general.

2.1.1.1 Kirbas summary

Kirbas et al. [11] divides vascular mapping strategies into six fundamental approaches: pattern recognition, model-based, tracking-based, artificial intelligence-based, neural network based and tube-like object detection:

1. Pattern recognition approaches

   Typically, pattern recognition techniques attempt to automatically detect or classify objects and features, an use general purpose image processing algorithms to extract those parameters. Some techniques are:

   - multiple-resolution analysis - For large complex scenes where it is not feasible to analyze the entire scene using one spatial or temporal resolution. Refining the resolution of the data, at specific areas of interest, aids in efficient processing and storage.
   - edge detection - going beyond simple edge detection to extract a derived line segment (skeleton or center-line). These techniques attempt to homogenize the data to facilitate linking segments together. Center-line approaches help with the final display of the reconstruction. It is more visually pleasing to travel down the center of a tube, than to bounce from side to side.
   - region growing - starting from some seed, regions are expanded and constrained by some criteria. Pruning of weak or small pathways occurs when the signals fall below the noise thresholds.

- filters and other mathematical schemes - uses differential geometry to extract parametric surfaces (or higher dimensional features) to establish relationship or connectivity criteria for the collection of small segments. Normalizing the contrast and brightness and spatial size of images, especially from MRI or CT scans, is necessary to reduce artificial gradients impacting the reconstruction.

2. Model-based approaches

   Kribas et al. [11] divides model-based approaches into four categories:

   (a) Deformable model

      i. parametric models - attempt to find objects using parametric curves that minimize an energy model by actively adjusting contours (aka snakes).

      ii. geometric models

   (b) Parametric models - attempt to define objects parametrically and connectivity constraints are based on overlapping ellipsoids. Multi-scale models and volumetric techniques are utilized.

   (c) Template matching - utilized an *a priori* model to guide contextual matches.

   (d) Generalized cylinders - a variation of parametric models that is drawing significant research attention. Each segment is modeled as an elliptical tube and are linked together.

3. Tracking-based approaches

   Identifies regions of an image that contain good candidates for tracking. Various methods from edge detection, clustering, graph theory and maximum-likelihood criteria are utilized.

4. Artificial intelligence-based approaches

   Uses knowledge-based systems to exploit *a priori* information about the anatomical structure. This information is used to guide the segmentation process and reconstruction. Systems in this category are generally rule-based expert systems. They are large and employ many algorithms.

5. Neural network-based approaches

   Neural networks provide a system to cluster or classify data of high dimensionality to a dimension more manageable. Neural networks are configured using supervised training, wherein a data set is reserved for training the neural network or unsupervised training, wherein the network does not depend on a training set. Neural networks facilitate the identification of non-linear relationships in the data. Neural networks, are excellent noise filters. At the risk of over generalizing, the basic rule-of-thumb, when it comes to neural networks, is: "use them to classify non-numerical relationships."

6. Tube-like object detection

   This feature detection methodology aims to model the blood vessels as tubes. Various techniques of edge detection and contour matching are applied to generalized cylinders.

2.1.1.2 2D Intravascular ultrasound

Intra-vascular ultrasound (IVUS) techniques described in [15, 11, 3] may produce greater 3-D resolution due to the in-vivo examination of blood vessels. Research to determine the location and orientation of the catheter tip, where the ultrasound device is located, is on going, and some early work that uses fiber optic cables is described in [16, 17]. Those systems, however, use light emitted from the fiber as a beacon that shows up on MRI scans. Therefore, the tracking is remotely sensed. Another system

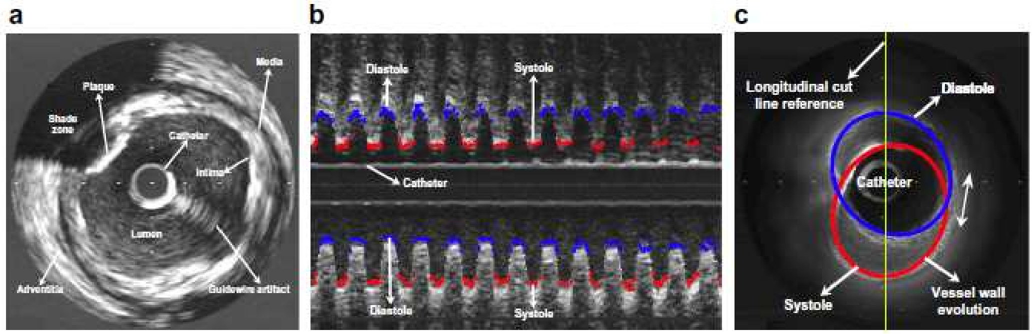

Figure 2.1: Morphological arterial structures and artifacts in an IVUS image (a). Sinusoidal shape in a longitudinal cut (b) and grey-level shift in cross sectional view (c). Red and blue ellipses show the location of vessel wall at systole and diastole, respectively [20].

uses radio frequency (RF) fields to track the catheter tip [4]. Finally, commercially available RF systems that track catheter tips are available from Ascension Technologies [18] and later improved [19]; they use radio triangulation, which requires two or more external RF field generators.

Unless the data are properly "gated" or synchronized with the cardiac motion, the sequence of images can take on a "saw-tooth" appearance. Substantial image processing is required if non-gated data is used. Additionally, the catheter orientation is not guaranteed and can twist during the "pull-back" (retraction) data collection. Rosales et al. [20] presents techniques for correcting for cardiac activity, blood vessel motion and catheter rotation. Figure 2.1 illustrates some of these challenges.

Integration of cardiac X-ray images and cardiac magnetic resonance (MR) images acquired from a combined X-ray and MR interventional suite (XMR), along with optical tracking are used to reconstruct the 3-D position of a point or line from a pair of X-ray views, and transfer this 3-D structure into MRI coordinates[21].

The research of Subramanian, Thurbrikar, Fowler and Mostafavi[3] relied on the hand selection of catheter tip locations as the mechanism to construct the set of 3-D coordinates necessary for the accurate 3-D volumetric reconstruction of the arterial vessels.The process involved the capture of two X-ray fluoroscopy videos to locate and track the catheter tip; where the IVUS sensor is located. Much of the early processing steps involve manual identification of the catheter tip location. There has been limited success in automating this process due to the poor quality of the X-ray video data. Subsequent processing, for accurate 3-D reconstruction involves correcting for bi-plane displacements, adjusting the center-line, and interpolating for missing data due to sampling rates. Once the reconstruction is complete, standard slice and dice manipulation can permit the virtual exploration of the vessels. Figure 2.2 illustrates the difficulty of visually locating the catheter tip, even under the most ideal conditions, requires a considerable image processing effort. Image noise, low contrast and even the contrast fluid can obscure the catheter. While it is possible to locate and track the catheter tip, current techniques are not reliable and require some "human" intervention or guidance. Typically, such systems can not perform in real-time.

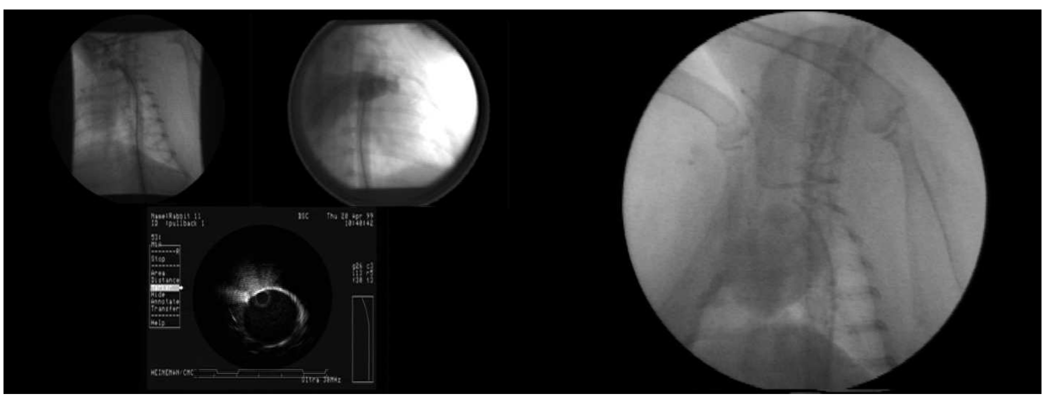

Figure 2.2: A synchronized view of two x-ray and the ultrasound data (left) shows contrast and image formats must be considered during analysis. A close up of one x-ray video frame (right) illustrates that, even under ideal conditions, the catheter is difficult to see and its position difficult to analyze.

While analyzing stereo X-rays video is a viable and workable solution it is not without problems. First and foremost is the use of X-rays. Second is the quality of the data. Also, the X-ray imagery suffers from noise, low contrast and requires powerful image processing systems. Finally, X-rays require special operational safety

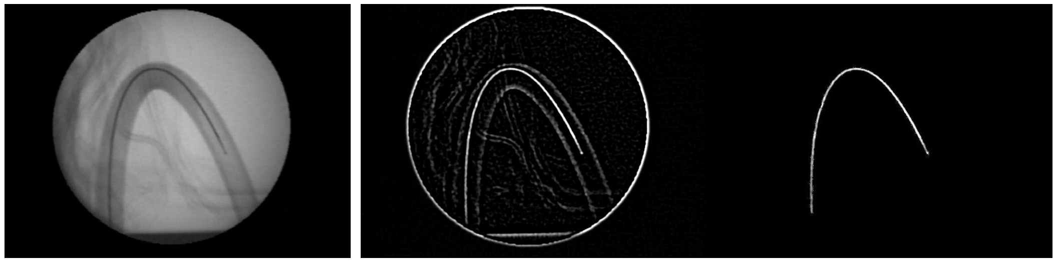

(a) Sensor data. (b) Initial processing of sensor data. (c) Catheter only

Figure 2.3: A laboratory setting for analytically determining the catheter path is aided by good contrast of the x-ray image (a), followed by contrast enhancements and edge detection (b) and using temporal changes as the catheter path is extracted (c).

requirements. The validation dataset will consist of catheter paths. More specifically, the mean of a sample population of catheter paths. In the laboratory, the curves will be ideal and not exhibit "saw-tooth" characteristics as illustrated in figure 2.1. Regardless, though, the analysis is the same.

Figure 2.3 illustrates one example processing scenario for extracting the path of the catheter, in a laboratory setting. The catheter is inside a plastic tube. Using frame to frame motion detection, the catheter tip is easily located. From that, the entire catheter path is constructed.

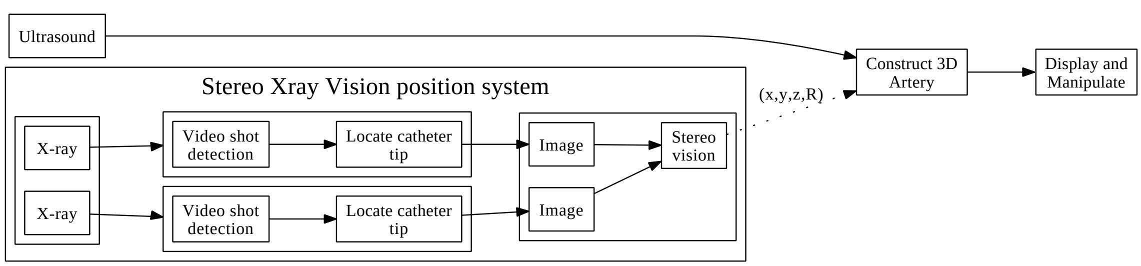

Figure 2.4: System architecture for the IVUS 3D vascular reconstruction described in [3].The two xray views are stereoscopically analyzed to compute the position of the IVUS sensor co-located at the catheter tip.

The position of the IVUS catheter, in the system of Subramanian et al. [3], is computed from the analysis of a stereo x-ray vision system, shown in figure 2.4. Each point, in each view, has a corresponding (x, y) and when combined, along with camera calibration parameters, the depth, or z, is computed. Let (x_l, y_l) be the pixel coordinates in the "left" image. And, similarly (x_r, y_r) for the "right" image. And let f be the focal length of the two cameras. If b is the distance between image centers of the two camera, then we get[22]:

$$z = \frac{bf}{x_l - x_r} \tag{2.1}$$

This, of course, assumes that there is no disparity in the y direction and that the cameras are identical. In practice that is not the case. The cameras are different and their image planes have an arbitrary orientation. In this case, a full camera calibration matrix is needed. The camera calibration system of Roger Tsai is recommended[23].

2.1.2 Summary of vascular reconstruction

The literature illustrates that it is not only important to identify the location of the catheter tip (the IVUS location), but it is also important to track its motion.

Generally, the process of 3-D vascular reconstruction of IVUS data involves the video capture of X-ray fluoroscopy to locate and track the catheter tip; where the IVUS sensor is located. Much of the early processing steps involve manual identification of the catheter tip location. There has been limited success in automating this process, due to the poor quality of the X-ray video data. Subsequent processing, for accurate 3-D reconstruction involves correcting for bi-plane displacements, adjusting the center-line, and interpolating for missing data or sparseness due to sampling rates. Once the reconstruction is complete, standard slice and dice manipulation can permit the virtual exploration of the vessels.

The CardiOp-B® system performs 3-D reconstruction of arteries in real-time using two or more angiography images[12]. Additionally, it provides quantitative vessel analysis yielding accurate 3-D geometric measurements. Essentially, the CardiOp-B® provides an external view of the arterial structure. The IVUS system, on the other hand, provides an internal view of artery vessels and can peer into the soft tissue of the arterial wall. IVUS provides adequate views of stenosis and plaques. A possible system that combines both the CardiOp-B® with an IVUS system would provide a complete view (both an external and internal) of the arterial structure. Such a system does not exist today. The missing ingredient for that combination is a set of 3-D coordinates, (x, y, z) of the ultrasound data (each image) along the entire length of the catheter pathway. The importance of co-locating the IVUS tip to angiography images, like those from CardiOp-B®, is not known, but over 66% of stents are not placed correctly[1]. This literature survey would suggest that combining IVUS and angiography would be one way to improve diagnosis and treatment.

2.2 Fiber optics

Light propagates in a medium, that is enclosed by another medium of a lower index of refraction, indefinitely and bounded by optical energy absorption of that medium. Such a construction is called a waveguide. This principle has guided research to develop fiber optic cables. These cables are composed of pure silica core surrounded by a cladding of a lower index of refraction silica, which permits the propagation of light waves wholly within the fiber; via the principle of internal reflection.

The following subsections provide a survey of literature in the field of fiber optics as they pertain to analyzing modal patterns toward the application of accelerometers.

2.2.1 Literature survey

The "City of Lights"[24] is an excellent and non-technical introduction to fiber optic technology. It covers the entire history of fiber optic research and development beginning with internal reflection water fountains as a visible and entertaining attraction to the theoretical calculations, performed by Charles Kuen Kao and George A. Hockham, to determine the maximum distance (signal loss) that light can propagate along a fiber. The race to construct the best fibers and to string them across the country and across the oceans is a captivating storyline and you feel the same sense of urgency that researchers felt as they struggled to complete fiber roll-outs to meet deadlines.

In 1965, Charles Kuen Kao and George A. Hockham calculated the theoretical limits, based on the power of a laser transmitter and the performance of an optical sensor, that a 20 decibel loss would occur per kilometer for a cladded fiber. This means that 0.1 percent of the light entering the fiber would remain after a kilometer. However, the current state-of-the-art for fibers, at that time, was a 20 decibel loss over just 20 meters. Kao wondered what was the theoretical limitation using fibers in which all impurities were removed. Kao and Hockham conducted experiments and determined that the theoretical goal of 20 dB loss was attainable, practical and inexpensive to fabricate and in 2009, Kao was honored with the Nobel prize in Physics[24, 25] for this work.

The wavelengths in the visible spectrum are from 0.4 μm to 0.7 μm, the near infrared are about 0.85 μm, and long wavelengths are considered 1.1 μm to 1.6 μm. In the visible spectrum, the fiber losses are moderately high, so only short links are practical. Near 0.85 μm, glass attenuation is moderately low and light sources and detectors are abundant and inexpensive. Better transmission efficiency occurs at the longer wavelengths. For these reasons, the long wavelengths (1.3 μm and 1.55 μm) are suitable for long paths and large information rates[26].

Plastic, rather than glass, fibers are available for short path length. These fibers are restricted to short lengths because of the high attenuation in plastic materials. Plastic fibers are designed to have high numerical apertures (typically, 0.4–0.5) to improve coupling efficiency, partially offsetting the high propagation losses[27]. Roboticists use plastic fibers.

The maximum acceptance angle, for a fiber wave guide, is determined from:

$$tan\theta = \frac{d}{2f} \tag{2.2}$$

where d is the diameter of the fiber, f is the lens focal length. Because of circular symmetry of the fiber, it will receive light within a cone having half θ. The numerical aperture (NA) is defined to be:

$$NA = n_0 sin\theta \tag{2.3}$$

where n_0 is the refractive index of the fiber, and θ is the maximum acceptance angle[28].

2.2.2 Interferometers

Fiber optic cables are primarily used for communication. However, several characteristics are present that can provide a host of other uses. Interferometry is the study of the interference patterns of the light waves as they travel along a fiber. Changing the shape and and causing physical distortions, of the fiber, effects changes in the interference patterns of the light waves as they propagate. Correlating the events that cause the fiber distortions, with the interference patterns resulting, is interferometry. Physical processes that can be measured with fiber cables are: pressure, presence of fluids, bending, temperature, vibration, etc. Some interferometers are simple and inexpensive to construct. Those that are simple or inexpensive generally sacrifice precision or require more processing.

The sections that follow discuss the various characteristics of six of the more popular interferometers and what types of measurements they are most suited.

2.2.2.1 Multi-mode fibers

The term multi-mode refers to the multiple pathways photons of light propagate through a fiber. The numerous waves of light cause constructive and destructive

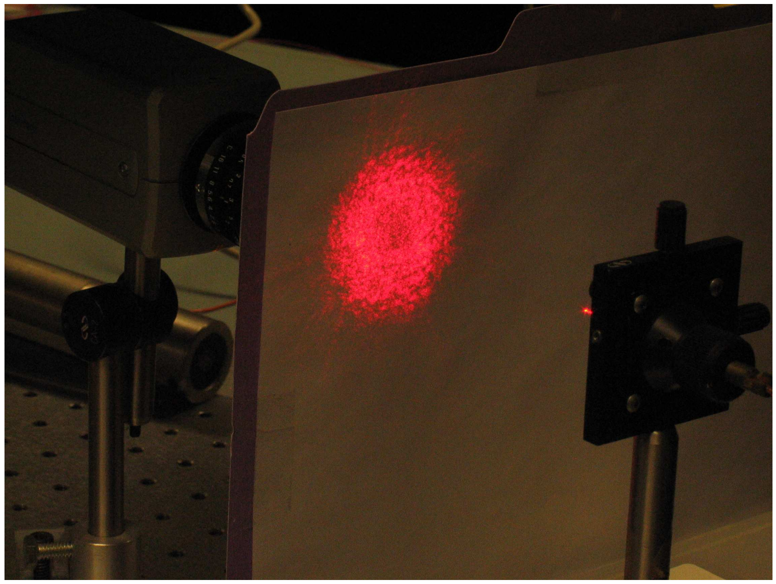

Figure 2.5: The specklegram is projected onto a tracing paper screen which attenuates the bight HeNe laser ($633nm$) light emitted from the end of the multi-mode fiber cable. A microscope camera images a small section of the specklegram. Each point of light is a mode. Many thousands of modes are present.

interference resulting in bright and dark patterns within the fiber. Those patterns of light, at any cross-sectional point along the fiber, are called a specklegram. Or, a specklegram is a projection of light emitted from the multi-mode fiber onto a screen; the specklegram is thousands of small clusters of light, called modes. Figure 2.5 shows the full projection of the specklegram onto a sheet of paper (the screen). Figure 2.6 shows a small section of the specklegram, captured with a microscope video camera.

Multi-mode transmission is complicated. Not only do you have many modes on a cross section of fiber, but the modes travel at differing speeds (actually, along differing path lengths). For communication, the bandwidth is restricted by the length of time all modes in a pulse take to reach the target. You can think of this as a temporal bandwidth. The more modes you have the more temporal lag you have and thus, reducing your data transmission rate. For single-mode fibers, the temporal dispersion does not exist and, thus, does not affect the data transmission rate. For telecommunications, single mode fibers are desirable for exactly that reason. Secondly,

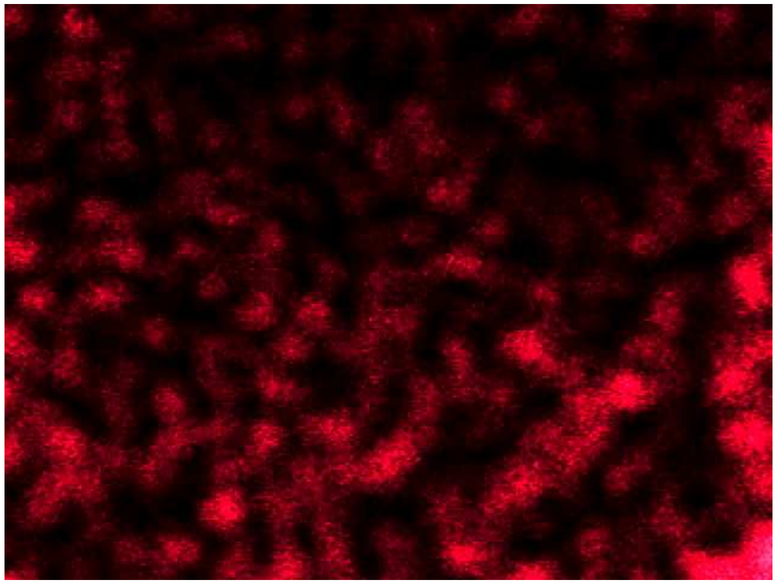

Figure 2.6: A microscope camera images a small section of the specklegram that has been projected on a tracing paper screen. Each point of light is a mode. Only a few hundred modes are needed for analysis. The specklegram pattern changes in direct reponse to fiber movement (bending, strain, etc.).

for single-mode fibers, bending or twisting the fiber does not affect the shape or distribution of the modes; there is only one mode. This dissertation, however, is attempting to extract physical parameters (bending, twisting) from the change in mode shapes or distributions. Because a single-mode fiber is immune to physical changes, it is precisely why it is not suitable for measuring acceleration; for this dissertation. The change in modal patterns, due to fiber bending or twisting, is a necessary component for extracting magnitude of bend and degree of twisting.

2.2.2.2 Modes in step-index fibers

A step index fiber has a uniform index of refraction within the core and decreases near the core-cladding boundary. The number of modes in a step-index fiber is approximately, and when $V > 10$:

$$N = \frac{V^2}{2} \tag{2.4}$$

where

$$V = \frac{2\pi a}{\lambda}\sqrt{n_1^2 - n_2^2} \tag{2.5}$$

where λ is the wavelength, a is the core radius, and n_1 and n_2 are the refractive indexes of the core and cladding, respectively[29]. If $V < 2.405$, then the fiber is considered single-mode. Otherwise, it is a multi-mode fiber[30]. You can reduce V by reducing the core radius or the numerical aperture (NA).

$$NA = \sqrt{n_1^2 - n_2^2} \tag{2.6}$$

The change in the speckle pattern, due to fiber stresses, can be tracked and associated with those stresses. This thesis presents the theory that there is a one-to-one correspondence of stress parameters to speckle patterns. While it is possible for a many-to-one, one-to-many or a many-to-many mapping, it is unlikely, for short, "real" (imperfect) fibers. Gangopadhyay et al.[31] says that the research on fiber Bragg grating sensors has occurred over several decades. It is reasonable to assume that the research on a multi-mode fiber accelerometer may take as long.

2.2.2.3 Fiber Bragg Grating (FBG)

Fiber Bragg gratings are obtained by creating periodic variations in the refractive index of the core of an optical fibre. These periodic variations are created by using powerful ultraviolet radiation (holographic method). In a single mode optical fiber, light travels in the fundamental mode along the axis of the core of the fiber. When light passes through an FBG, Fresnel reflections take place due to the variations in refractive index of the fiber. This is called coherent reflection[31].

The main advantages of FBGs over other optical sensor schemes are its low cost, good linearity, wavelength multiplexing capacity, resistance in harsh environments and absolute measurement. FBG sensor technology is now on the verge of maturity after almost two decades of active research and development in this field. Efforts are now concentrating on delivering complete FBG sensor systems including front-end electronics[31].

Fiber Braggs Grating (FBG) is governed by the principle of Fresnel reflection, wherein as light travels between two materials having different refractive indexes, both reflection and refraction occur at the boundary. Usually, it is the reflective wavelength that is useful. The reflected wavelength, λ_B, also known as the Bragg wavelength, is defined by:

$$\lambda_B = 2\eta_e\Lambda, \tag{2.7}$$

where η_e is the effective refractive index of the grating in the fiber core and Λ is the grating period. Thus, they are useful as strain and temperature sensors[32].

Fiber strain sensors are constructed using several gratings along a single fiber, each grating reflecting a unique λ_B. As the fiber bends, or strained, the reflected frequency is modified, $\lambda_B \pm \epsilon$. Provided that the other grated segments of the fiber do not overlap this range (bandwidth), then the location of the strain is unambiguous and ϵ indicates the amount of strain.

2.2.2.4 Neural Network-Based Analysis

Marusarz and Sayeh[33] demonstrate that multiple overlapping signal frequencies (colors of light) can be inserted simultaneously into a multi-mode fiber and accurately demodulated to extract the original signals (or colors). This increases the multi-mode fiber transmission rates by a factor of 6.

Also, Sayeh et al.[34] illustrates strain measurements are possible using real-time neural network processing of speckle patterns of embedded multi-mode fibers.

If the signals represent different physical measurements, it may be possible to multiplex them into a the multi-mode fiber and then to de-multiplex them (separate them), without loss. For instance, if different frequencies represented orthogonal acceleration measurements, then it could be possible to determine the acceleration in each direction. This is essentially what a Fiber Bragg Grating does, but multiple fibers are needed. Therefore, it may be possible to construct an accelerometer by analyzing the speckle patterns of a multi-mode fiber undergoing stress due to movement under acceleration; this possibility is the focus of this dissertation study.

2.2.2.5 Other interferometers

These interferometer technologies were candidates for the medical application of tracking a cardiovascular catheter tip. While this dissertation chooses the multi-mode interferometry approach, these technologies are worth pursuing as possible solutions for the aforementioned application. Schematics for experimental setups and product setups, for each of the following, are presented in appendix A.

1. Fabry-Perot: Measure the interference patterns resulting from multiple reflections between two reflecting surfaces. A highly sensitive accelerometer combining Fabry-Perot technology with MEMS technology on a semiconductor integrated circuit, demonstrated world-record sensitivity[35].

2. Michelson: Best known for measuring special relativity and gravitational waves. See Laser Interferometer Gravitational-Wave Observatory (LIGO).

3. Mach-Zehnder: Measures the phase shift of two beams from a laser. The phase shift, for instance, can be due to the differing path lengths of two beams (split from one).

4. Jamin interferometer: It is closely related to the Mach-Zehnder interferometer and displacement (due to pressure, for example) can be measured as interference fringes.

5. Polarimetry: Measures interference patterns due to changes in polarization.

6. Chirp Grating: Uses a broadband laser to transmit varying frequencies of light pulses, then measure the changes in the pulse frequencies.

2.2.3 Fiber Accelerometers

Using fiber cables as accelerometers has been studied using numerous configurations of fiber construction, as well as, numerous integration configurations. The simplest model to describe is a fiber that reacts to motion in a mass-spring configuration as described in [36, 37] and [38]. One such mechanical system that employs a Michelson fiber interferometer for constructing an accelerometer is illustrated is described[39]. For a broad overview of fiber optic sensors, see [40].

Accelerometers are devices that measure acceleration, usually in one dimension. When three accelerometers are placed orthogonally to each other, then measuring acceleration in 3-space is possible. Accelerometers found in everyday devices: cell phones, game wands, and automobile air-bag switches, are the size of a grain of rice and are micro-electromechanical machines (MEMS) constructed using integrated circuit manufacturing techniques[41]. A gyroscope is a special type of accelerometer that reports rotational accelerations. When a gyroscope and an accelerometer are combined, all six degrees of freedom are measured.

Generally, accelerometers measure mechanical movement. The object that moves and is measured is called a "proof-mass". These "proof-masses" can be sliders, pendulums, springs, etc. The accelerometer is calibrated based on the movements of the "proof-mass", which returns to its unaccelerated position when no acceleration force is present. One example of a fiber optic accelerometer employing a "proof-mass" or a "mass-spring" system is [38], see figure 2.7.

An accelerometer with a proof-mass on a vibrating diaphragm is discussed in [42], but differs from the approach in this dissertation in that it uses a moving mirror

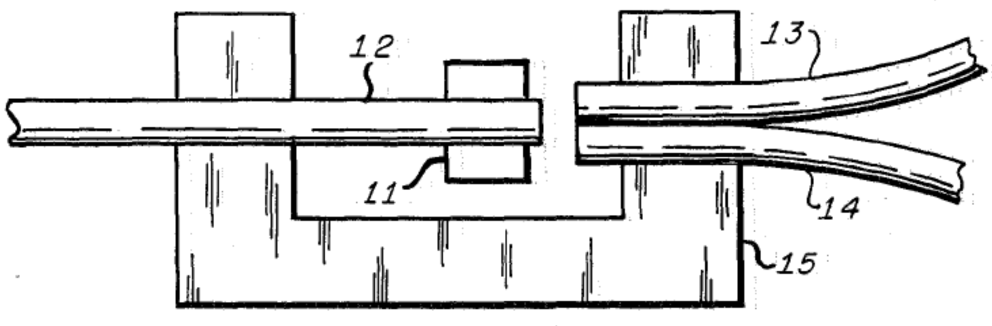

Figure 2.7: Multi-mode fiber “mass-spring” accelerometer. US Patent 4595830. Light enters fiber 12 and is deflected, based on the movement of the “proof-mass”, to fibers 13 or 14.

for the interferometry; it is a type of miniature hemispherical air-spaced Fabry-Perot interferometer. This device has the potential to be physically small, making it suitable for in vivo catheter tracking applications, see figure 2.8. However, this device measures only one axis of acceleration.

An alternative intensity-based sensor configuration for vibration measurement sensor is shown in figure 2.9[43]. The design uses two multi-mode ($50\mu m/125\mu m$) fibers for signal transmission, and a movable reflective surface for signal transduction. The device is a simple proximity sensor in which the displacement of the reflective surface is encoded as a variation in signal intensity caused by changing light path length between the two fibers. This sensor has a demonstrated displacement measurement range of 4.5mm with a resolution of better than 25 μm. This accelerometer measures only one axis of acceleration.

This is an example where multiple axis of acceleration is needed in a single device. This dissertation discusses how to make such a device using a single multi-mode fiber. A mass-spring approach is needed to provide a directional vector for the acceleration.

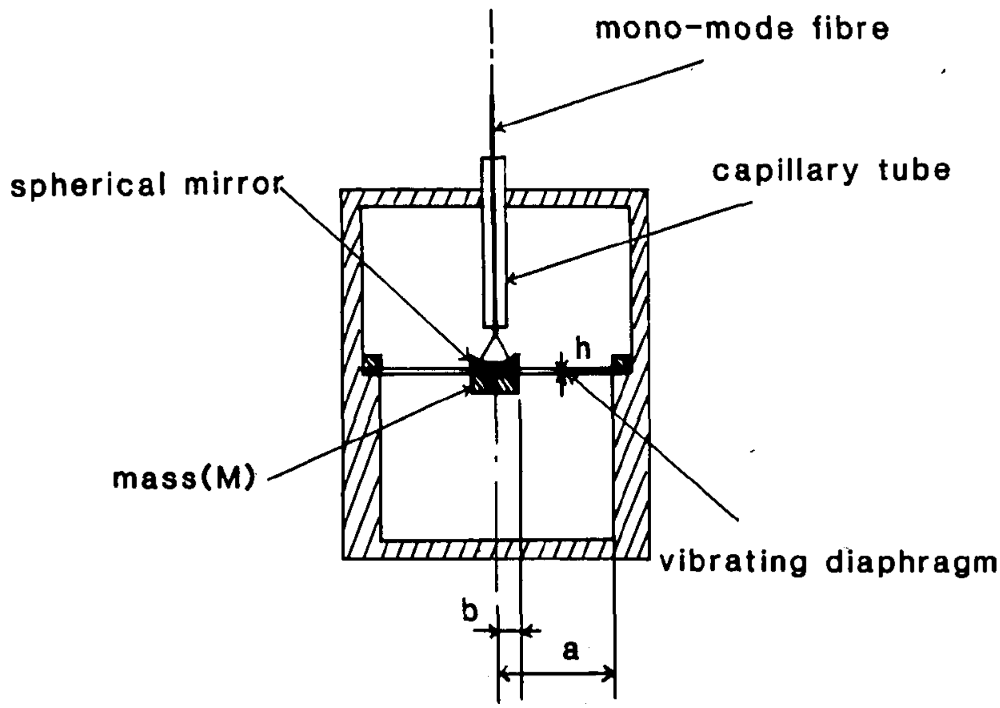

Figure 2.8: A schematic of a Fabry-Perot type single axis optical accelerometer that uses a vibrating diaphragm to affect a frequency change of the light reflected into the single-mode fiber.

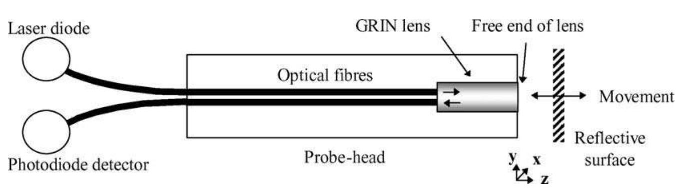

Figure 2.9: A schematic of an intensity-based multi-mode accelerometer sensor wherein the movement of the reflective mirror affects measurable changes in the path length of light reflected back toward the photo-diode detector.

2.2.4 Fiber optic strain sensors

Similar to accelerometers, strain sensors measure movement and translate it into a force measurement on the sensor. This differs from an accelerometer in that the strain can continue to exist even though there is no velocity or acceleration. Strain sensors can be used to measure the weight of objects, the squeezing force or the bending of objects. Constructing interferometers with fiber optic cables is a popular method of building strain sensors.

Using fiber optic cables to sense shape deformation with various interferometer or grating approaches has many applications. For example, Lunwei, Jinwu, Linyong and Yanan[44] use Fiber Bragg's Gratings to reconstruct the 3-D shape of a colonoscope. Techniques using long period gratings (LPG) can now determine location and orientation [45, 46].

Other fiber bend sensors are mentioned in a comprehensive collection of fiber sensors[47]. In particular, the book discusses using quasi-distributed Polarimetry as possible way to construct a shape sensor and illustrates a plurality of Mach-Zahnder interferometers to construct a shape sensor. Subsequently mentioned are fiber grating techniques that have produced numerous methods for creating shape sensors. Embedding a temperature, pressure and strain sensor into structures, for instance, is a popular application of the Fabry-Perot resonator. And, to construct a displacement sensor, white light must be transmitted down the fiber, again see [47].

Recently, neural networks have been utilized to create a fiber optic strain gauge with high sensitivity[48]. From that, it may be possible to apply a fiber optic strain gauge to measure the bend angles on a bundle of three fibers, provided the rate of transverse motion is known.

Further exploration of using fiber cables as a strain, or shape, sensor were carried out at UNCC in 2007[49]. It was demonstrated that it is possible to use a multimode fiber as a shape sensor. While a fiber sensor of this type is sensitive to minute

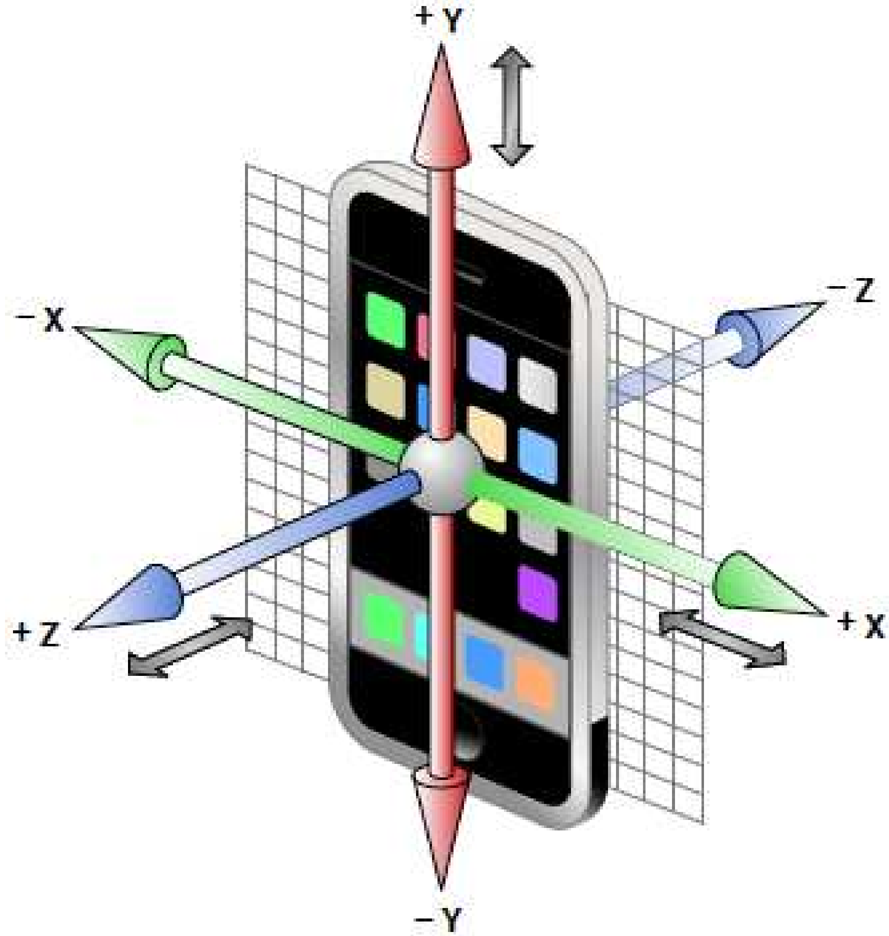

Figure 2.10: The iPod® contains an LIS302D tri-axial accelerometer constructed using MEMS fabrication technology. Moving the iPod® causes a change in the accelerometer reading on any or all three axes. It is subject to electromagnetic interference, most of which is caused by the mere operation of the iPod®. However, this device is sensitive enough to function as a validation sensor.

movements, calibration is daunting and computationally expensive.

2.3 MEMS accelerometer

The Apple Inc. iPod® contains a 3-axis accelerometer. See figure 2.10. This accelerometer will provide the data for evaluating the fiber accelerometer. While the accelerometer is subject to electromagnetic noise, predominately from its own electronic circuitry, it is sensitive enough and has adequate fidelity to be a validation sensor.

CHAPTER 3: METHODS AND EXPERIMENTS

This research investigates fiber technology and presents experimentation to support its suitability for tracking an IVUS sensor in vivo. This device has the potential of revolutionizing cardiovascular disease diagnosis and treatment. The intended device is small, inexpensive to manufacture, and provides immediate positional readout of the location in 3D space.

This chapter introduces a device based on fiber optic accelerometer technology, with detailed schematic drawings. A discussion of how the output from the device will be compared to existing accelerometers follows. Utilizing statistical analysis of variance, a criteria for determining the performance of the fiber accelerometer is established.

3.1 Introducing a fiber accelerometer

Multi-mode speckle patterns are very sensitive to fiber movement and also sensitive to fiber twisting. These are two features of a position sensor: detect movement and detect orientation. Another word for a position sensor, in this document, is an accelerometer.

Accelerometers fall under a category of devices known as inertial sensors. Just as the name implies, inertial sensors detect and measure inertia. This insight comes Newton's first and second laws of motion. The first law states that "a body at rest will remain at rest" and "a body in motion will remain in motion." The second law states that "if a force is applied to a mass, then the mass undergoes acceleration". Mathematically, the two laws are combined into one equation: $F = ma$; force equals mass times acceleration. Restating, "if a force is applied to the fiber cable, then it is undergoing acceleration." To calculate position from acceleration at any point in time, $p(t)$, integrate twice:

$$p(t) = \int v\,dt = \iint a\,dt \tag{3.1}$$

where, $v(t)$, is the velocity at any point in time, and:

$$v(t) = \int a\,dt \tag{3.2}$$

There are three properties of a multi-modal fiber that can be mathematically combined to construct a unique and practical fiber accelerometer:

1. The modes deform and change position when the fiber is bent or squeezed.

2. The amount of deformation is easily measured and tracked with non-linear mathematical models. Qualitative and quantitative values are obtained from those models.

3. The entire modal pattern (speckle-gram) rotates in response to fiber twisting; suitable for a gyroscopic analysis. Changes in the speckle pattern indicate how much force, including torque (twisting), is being applied. Gyroscope analysis was not conducted in this dissertation.

Figure 3.1 depicts the expected displacement of the speckle image after acceleration in x. There are two possible sources for determining the acceleration:

1. Use a neural network to measure the speckle pattern deformation and translate that to acceleration.

2. Use the displacement directly and apply the physical constraints of the "mass-spring" to measure acceleration.

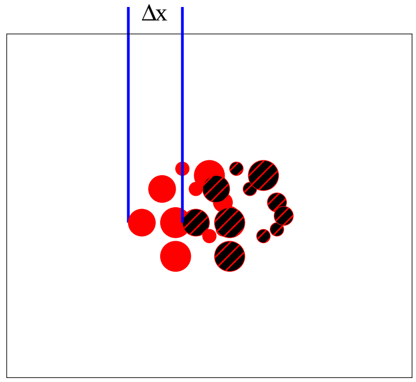

Figure 3.1: Image displacement of the multi-mode fiber; used as a "mass-spring", under acceleration.

Measuring the displacement Δx may be subject to resolution constraints which would limit the possible values for Δx. This would produce a set of values $\{x_1, x_2, \ldots, x_n\}$. The neural network result could provide a higher fidelity and fill in the values between Δx's. The final set of measurements is $\{x_1, \mathbf{Y_1}, x_2\mathbf{Y_2}, \ldots, \mathbf{Y_n}, x_n\}$, where $\mathbf{Y_1} = [y_1, y_{m_1}]$, $\mathbf{Y_2} = [y_1, y_{m_2}]$, ...

Measuring the displacement is necessary only to provide a directional hint. It should be sufficient that $\mathbf{Y_i}$ is all that we need. In fact, $\{x_1, x_2, \ldots, x_n\}$ may be all that is needed.

3.2 Fiber accelerometer device schematic

Figure 3.2 shows the experimental schematic to test the hypothesis. The "mass-spring" is attached to the multi-mode fiber segment and is free to move under acceleration influences. In the lab, a camera will measure the speckle pattern and displacements. As long as the multi-mode segment is short, it should function as an effective inertial sensor. Additionally, figure 3.3 is closer to the product schematic and where a "hint" to the direction of the "mass-spring" movement is detected.

However, a short fiber segment is impractical for in vivo catheter tracking. A single-mode fiber can provide stable light transmission and be coupled to the multi-

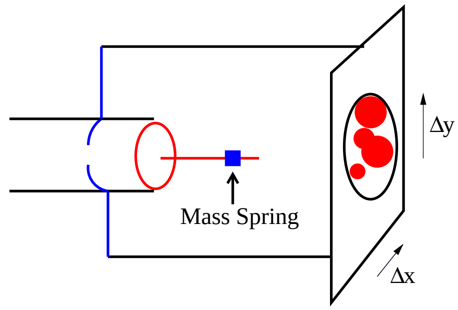

Figure 3.2: A schematic of the multi-mode fiber “mass-spring” accelerometer. The “mass-spring” moves due to the effects of acceleration and the modal patterns change accordingly. Two axes of acceleration are measured; the x and y axis. For the laboratory configuration, the specklegram is projected onto a screen and measured directly with a camera.

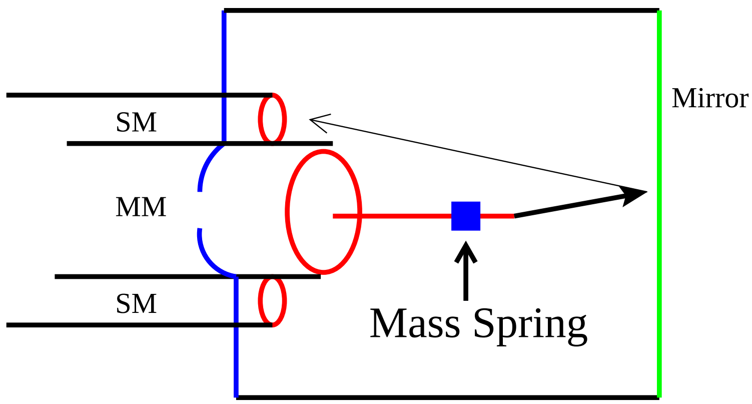

Figure 3.3: A schematic of a multi-mode to single-mode transfer replaces the projection screen in figure 3.2 with a mirror. Acceleration direction cannot be deduced from changes in the speckle pattern with this configuration, therefore single-mode fibers are used to provide the directional hint.

mode fiber. Single mode fibers are not affected by fiber bending, twisting or other stresses. The multi-mode end contains the “mass-spring”. Since a multi-mode fiber speckle pattern is affected by bending and twisting, both of which will occur during acceleration, it will measure the desired acceleration.

Statistical methods and experimental designs, to test the effectiveness and validate the position sensor, are presented.

Validation is critical to ensure that the “New Sensor” is performing as expected. Validation involves the comparison to known results. In order to do that, separate systems that produces identically formatted output to the position sensor must be constructed. A statistical comparison between the validation system and the "New Sensor" will determine the performance and give a measure of confidence for a successful comparison.

Ideally, the fiber position sensor will produce a set of $(x, y, z, \mathbf{R})$[1] at some sampling frequency. Those points are used to construct a curve. This curve represents the entire catheter path. It will be the two curves representing the two catheter paths, one from the validation, shown in figure 2.4, and one from the "new" position sensor, that will be compared. If the comparison says they match, then we have successfully validated the position sensor. If they do not match, then more work must be performed to adjust the operational parameters to bring the two system closer together. Figure 3.4 depicts the final system architecture without a validation system.

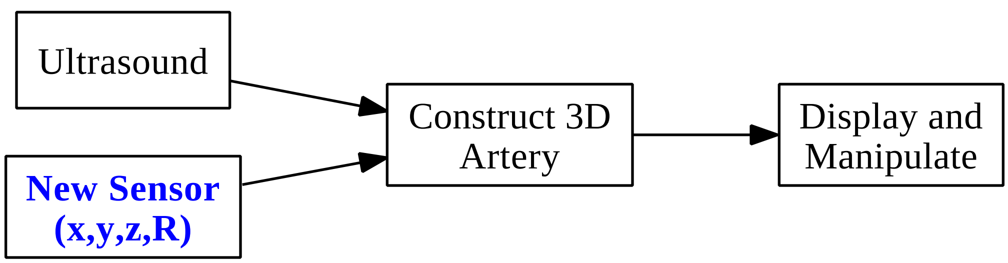

Figure 3.4: The system architecture is shown without the "Stereo Xray Vision position system" from figure 2.4, which would function as the validation sub-system.

While figure 3.4 depicts a comparison of position points, $(x, y, z, \mathbf{R})$, it is not what "New Sensor" is producing. The "New Sensor" is producing a measurement of acceleration. The position points are obtained from the double integration of the acceleration points. Therefore, the "New Sensor" is a combination of a fiber accelerometer with a double integration calculation. However, it will be sufficient to compare the accelerometer readings to a working accelerometer. Figure 3.5 shows the experimental architecture. To properly conclude that the fiber accelerometer can measure acceleration, four representative experiments are conducted.

[1] x, y, z are scalar values. $\mathbf{R}$ is a 3x3 rotational matrix. In the context of this dissertation, $\mathbf{R}$ is the identity matrix.

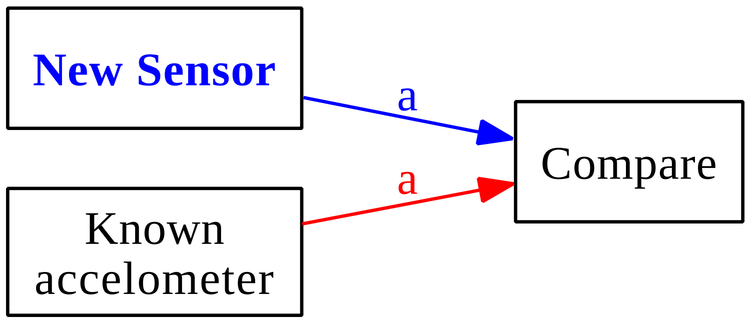

Figure 3.5: The system architecture depicting the validation of the "New Sensor" accelerometer reading, a, with a known accelerometer reading, a'.

3.3 Experimental Design

- The experimental design is a simple CR-1 (Completely Random with one degree of freedom).
- Use ANOVA T-test with a level of significance $\alpha = 0.001$; a 99.9% confidence interval.
- Similarly, compute the mean, μ, and standard deviation, σ, for the new sensor.

3.4 Compare two curves

To validate the new sensor, it is compared to the validation catheter path (or curve). If the distance and shape match, then validation is successful, otherwise it is a failure. Each curve in figure 3.6 represents the average from a population of curves (the error bars are not shown). Since each curve is a distribution, it is only necessary to compare the means and variances to determine if the curves are close and have the same shape.

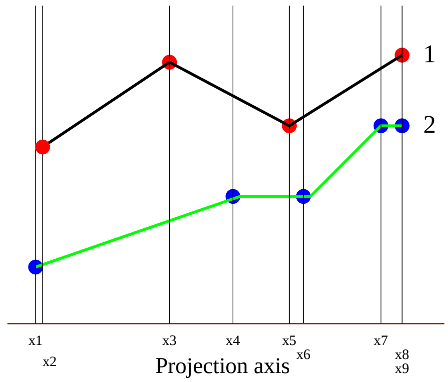

Figure 3.6: A graph showing the readings from the "New Sensor" (1) and the validation sensor (2). The mean and standard deviation of the absolute value of the difference between the curves (as a function of the projection axis; this case x) are used to determine if the curves match. The error associated with curve 2 also has a mean and standard deviation and can be considered the thickness of the line. If curve 1 lies within the error of sensor 2 (is close enough), then the curves are statistically indistinguishable. Analysis of variance (ANOVA) is used for this analysis.

The method to compare two curves is to:

1. Calculate the absolute difference at each sample point. This is non-trivial and figure 3.6 illustrates that there may not be a corresponding sample point in both curves for the same x value. In that case, new points will be computed via linear interpolation. For example, line 2 does not have a corresponding x_3 point from line 1.

2. Use those differences to construct a distribution.

Comparing the two curves consists of computing the distance between them and comparing their shape. Each line, L_1 and L_2, is a set of linear line segments:

$$L_1 : \quad \{y = f(x) = m_i x + b_i : i \in \{1..n-1\}\} \tag{3.3}$$

$$L_2 : \quad \{y' = f'(x) = m_j x + b_j : j \in \{1..m-1\}\} \tag{3.4}$$

The difference between each line segment produces a set P. Let $p = n + m$ to give:

$$P: \left\{ d_k = \sqrt{(f(x_k) - f'(x_k))^2} : k \in \{1..p\} \right\} \tag{3.5}$$

The mean distances between the two lines is then,

$$\bar{d} = \frac{1}{p} \sum_{k=1}^{p} d_k \tag{3.6}$$

and the shape similarity is the variance of those differences. If there is no difference, then $\sigma = 0$.

$$\sigma = \sqrt{\frac{1}{p} \sum_{k=1}^{p} (d_k - \bar{d})^2} \tag{3.7}$$

The confidence interval is defined about the mean:

$$(\bar{d} - \beta, \bar{d} + \beta) \tag{3.8}$$

and

$$\beta = \frac{3.291\sigma}{\sqrt{p}} \tag{3.9}$$

for the 99.9% confidence interval. Because the perfect match occurs when $\bar{d} = 0$, and $\bar{d} \geq 0$, the confidence interval becomes:

$$(0, \bar{d} + \beta) \tag{3.10}$$

Note,

$$\lim_{\bar{d}\to 0}(0, \bar{d} + \beta) = (0, 0) \tag{3.11}$$

for the perfect match. Alternately, from[50], the test statistic can be computed with

$$t = \frac{\bar{Y} - \mu_0}{\frac{\hat{\sigma}}{\sqrt{n}}} \tag{3.12}$$

where

$$\hat{\sigma} = \sqrt{\frac{\sum_{i=1}^{n}(Y_i - \bar{Y})^2}{n-1}} \tag{3.13}$$

to test the hypothesis $\mu \leq \mu_0$. $\bar{Y}$ is the mean of a random sample from the population, μ_0 is the mean specified in the null hypothesis, $\hat{\sigma}$ is an estimator of the population standard deviation, n is the number of elements in the sample used to compute $\bar{Y}$ and $\hat{\sigma}$, and μ is the unknown mean of the population.

3.5 Evaluation criteria

To evaluate how similar the lines L_1 and L_2 are, we use the null and alternative hypothesis tests. Let μ_1 and σ_1 be for the validation system. And, u_2 and σ_2 be for the new sensor paths. Then,

- The hypotheses test how close the curves are:

  $H_0 : |\mu_1 - \mu_2| = 0$

  $H_1 : |\mu_1 - \mu_2| \neq 0$

- And their shape is similar if:

  $H_0 : |\sigma_1^2 - \sigma_2^2| = 0$

  $H_1 : |\sigma_1^2 - \sigma_2^2| \neq 0$

Table 3.1: Criteria for accepting or rejecting the null hypothesis and the probability of a type-I or type-II error.

	H_0 true	H_0 false
Fail to reject H_0	Correct acceptance: $p = 1 - \alpha$	Type II error: $p = \beta$
Reject H_0	Type I error: $p = \alpha$	Correct rejection: $p = 1 - \beta$

The null hypotheses is accepted, by saying, "the two curves are mathematically indistinguishable from one another[2]."There are two possible errors. Selecting, α and β appropriately, will reduce the likelihood that these errors will occur:

- Type-I error is ok:
  - We say the curves are different when they are the same.
- Type-II error is not:
  - We say the curves are the same when they are different.

3.5.1 Experimental size and power

To determine the experimental size and power, which define the number of line comparisons needed, we use the standard analysis of variance equations, from [51]:

$$z_\beta = \frac{d(n-1)\sqrt{n}}{(n-1) + 1.21(z_\alpha - 1.06)} - z_\alpha \tag{3.14}$$

where

$$d = \frac{|\mu - \mu_0|}{\sigma} \tag{3.15}$$

[2]Commonly, in analysis of variance testing, the null hypothesis is rejected meaning there is a significant difference. While the test could be phrased that way, I am validating two curves, therefore I want the two curves to be similar; so, for the sake of clarity, I state the test that way.

CHAPTER 4: EXPERIMENTAL RESULTS

Four experiments, described in the following subsections, provide the necessary laboratory confirmation for the feasibility of the fiber accelerometer constructed using the design described in section 3.2 and illustrated in figures 3.2, 3.3 and 3.5. These experiments are a representative set, enough to prove that constructing a fiber accelerometer to provide positional information is practical; even though the current setup has limited accuracy, largely due to craftsmanship. The four experiments are:

1. Single Bend Sensor - Determine the amount a multi-mode fiber bends. The analysis will map speckle-gram patterns to distances the fiber is bent.

2. MEMS accelerometer - Perform an error analysis study for the iPod® MEMS accelerometer. It compares two iPod® accelerometers by measuring the differences of the total magnitude of acceleration (a combination of all three axes). Secondly, the x-axis accelerometer readings are analyzed. Also, this experiment studies the iPod® accelerometer sensor noise.

3. Fiber light transfers - This experiment determines the proof-of-concept that light from one fiber can be transferred to another over an "air-gap":

    (a) wherein there is no change in the primary direction of the light propagation.

    (b) wherein the light is reflected by a mirror before entering the second fiber.

4. Fiber accelerometer - This objectivees of this experiment are:

    (a) Construct a pendulum system that collects and measures the speckle perturbations while oscillating.

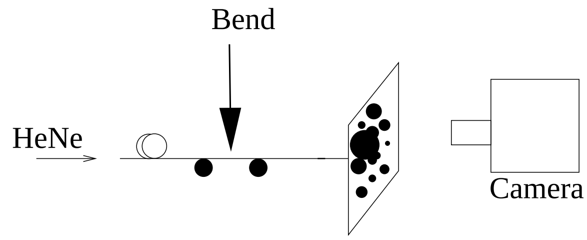

Figure 4.1: The single bend experimental schematic showing the bend location. The specklegram is projected onto a screen for detection by the camera. The light is a Helium Neon (HeNe) coherent laser with a wavelength of $633nm$.

(b) Validate the pendulum measurements using data collected from a real accelerometer; an iPod®.

(c) Use the statistics described in section 3.4 to compare the fiber accelerometer data with the iPod® accelerometer data.

4.1 Experiment 1 - Single Bend Sensor

A HeNe laser, $633nm$, is focused into one end of a $120\mu m$ multi-mode fiber[1]. The other end is clamped and extruded to shine on a diffusing lens. A microscope video camera is focused onto a small portion of the speckle image, to adequately discern the modes. A stage micrometer with a cylindrical rod attached is placed such that the rod moves the fiber which is suspended across two rounded platforms. All other locations of the fiber are taped down, to ensure that the micrometer moves the fiber in one location. As the micrometer is moved, the video is captured. See figure 4.1 and figure 4.2. Calibration and extraction of the training set of images occurs at known micrometer settings.

4.1.1 Empirical experimentation

Emperical investigation illustrates that there may be information in a speckle pattern that could be used to determine the shape of the fiber. As a multi-mode fiber moves and twists, merely by touching it, the speckle pattern changes and twists.

[1]The outside diameter for the cladding is $120\mu m$, the core diameter is $62.5\mu m$

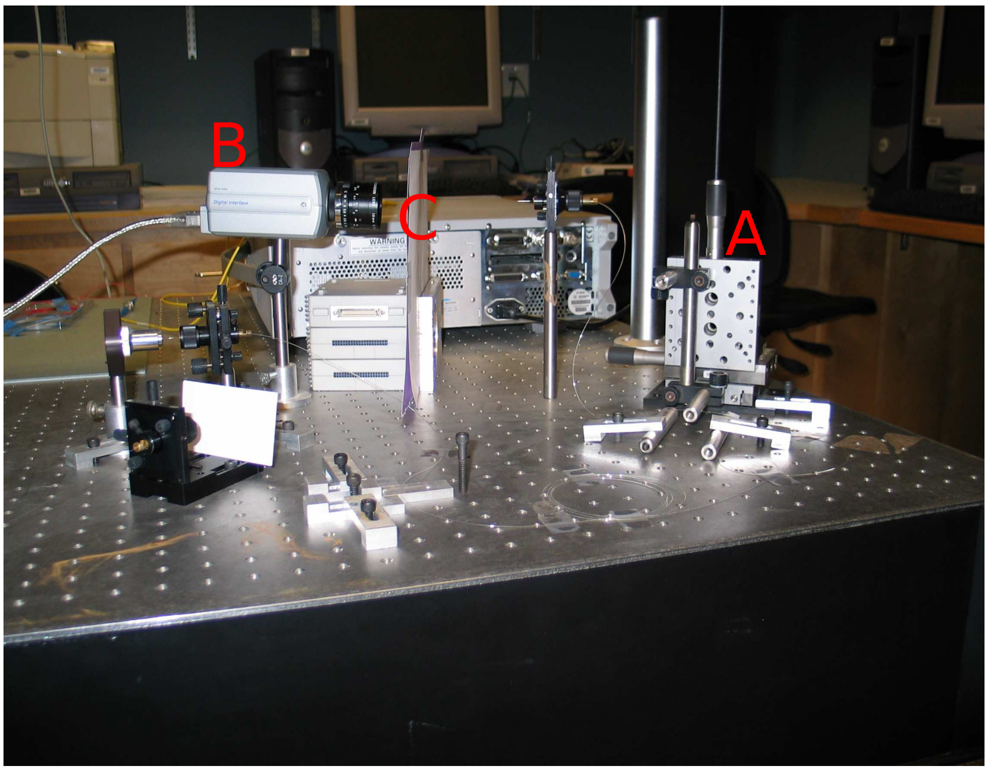

Figure 4.2: The single bend experimental laboratory setup utilizes a stage micrometer to bend the fiber (A). The specklegram is projected onto a tracing paper screen (C) for recording with a microscope video camera (B).

There are, of course, many degrees of freedom: temperature, air current, initial laser alignment, fiber stretching, friction, camera field of view, etc., that may limit reproducibility, but, if the final measurement resolution is coarse, (and tenths of mm may be coarse), then those variables may not be that important.

Any motion in the fiber, due to touching, squeezing, or twisting, yields gross movement of the speckle pattern. The fidelity is high, meaning that very small movements of the fiber are easily visible as movement of the speckle pattern. Additionally, the faster the fiber shape is modified, the faster the speckle image changes. Visually, the speckle change seems directly proportional to the rate of shape change. The same seems true for twisting rates.

In general, when the fiber was twisted, the speckle pattern also twisted. And when the fiber was bent, the speckle pattern showed changes, but did not twist, in general. That is, the pattern seemed to change in-place. Of course, a combination of twisting and bending produced visible twisting and in-place pattern changes in the speckle pattern.

4.1.2 Setup and data collection

The speckle pattern is analyzed using a feed-forward-back-propagation neural network. Intuitively, there are two things we want to track, as the speckle pattern changes:

1. The clusters, which are the modal points of the light waves.

2. The cluster motion due to fiber motion.

The input images are 640x480 pixel video images. They are converted from color to black and white, since the speckle pattern is mono-chromatic (red). When the fiber is moved, slightly, small changes in the speckle pattern occur, and it looks like the clusters, of the modal patterns, move as if it were fluid. For small movements of the fiber, the speckle movement seems to have continuity. Thus, in order to train the neural network to track these motions, it is necessary to provide a sufficiently high density of images so this continuity is not lost.

As the speckle pattern moves, so do the modal patterns. The clustering neural network is fed into a second neural network to track the motion of the cluster and associate them with known fiber displacements (movements). Instead of using two separate neural networks, we use a single neural network containing four – two hidden – layers.

- $320 \times 240 = 76800$ neurons. The input layer.
- 500 neurons. The clustering and noise filtering layer.
- 100 neurons. The cluster tracking layer. It classifies unseen images into one of these neurons.
- 1 SIGMOID neuron. Convert the 100 classifications in layer 3 into a floating point number along a SIGMOID continuous function[52].

More practically, though, the neural network is really functioning as an image database. The 20 images use to train the system are encoded in the neural network itself. Encoded with the images, is the set of bend points. Then, for all unseen images, the neural network determines which two images it is between, and computes a new set of bend points. Essentially, the new bend points are a weighted average of the position of the unseen image in the database. Figure 4.3 shows the speckle pattern arising from bending the fiber. Then, figure 4.4 shows the image database and the calculation of bend points for an unseen image.

From a database of 20 images, selected from a video sequence of approximately 600 images, the neural network was able to determine the bend distances for the entire video sequence. There is some binning of bend distances and this is, in part, due to the limited sampling for the training set and, in part, due to the limited complexity of the neural network; only 100 output neurons to classify distances.

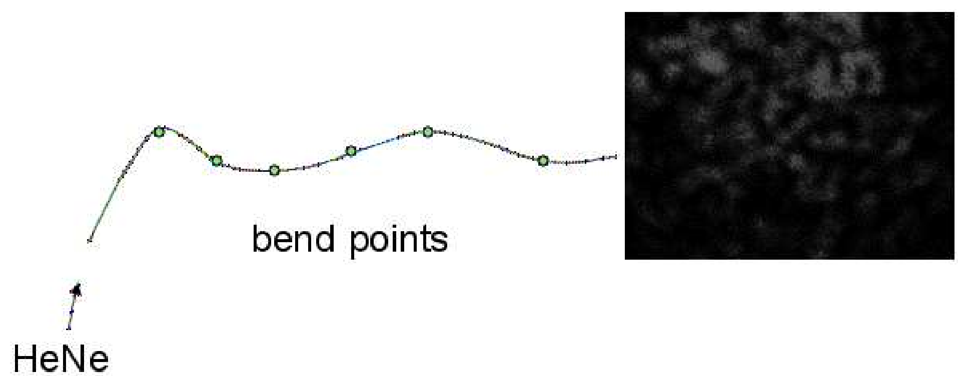

Figure 4.3: One possible specklegram pattern of a fiber. This experiment measured the bend at one location, but the system easily generalizes to multiple bend points. A collection of 20 images were selected as the training set for the neural network.

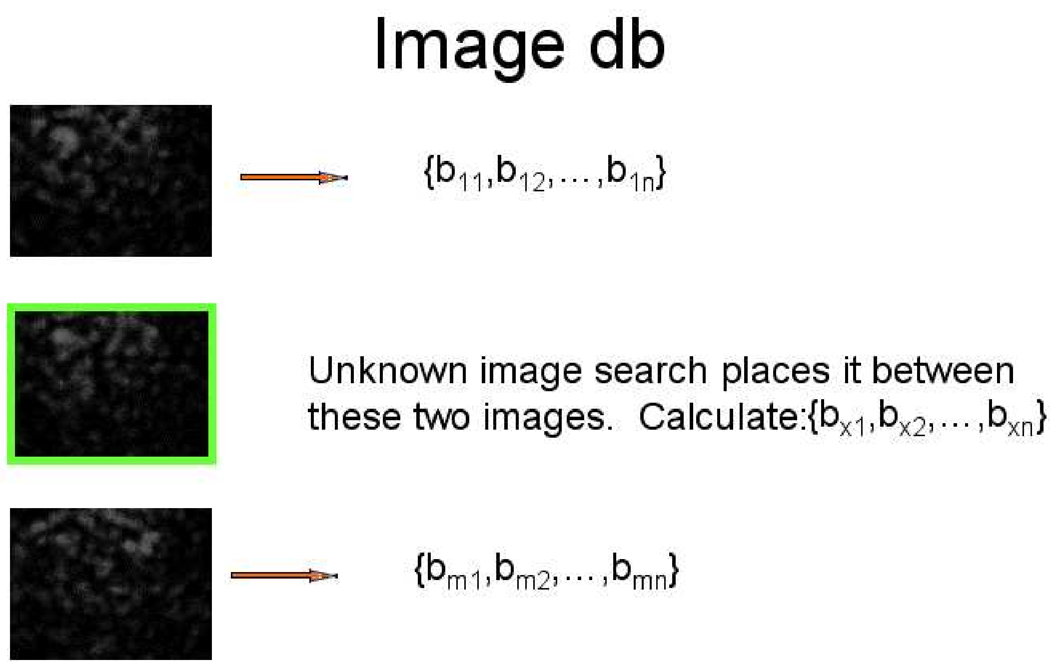

Figure 4.4: The neural network database of 20 images provides enough computational power to determine if an unseen specklegram lies between two images in the database. This computation is similar to linear interpolation; that's the effect. While the system generalizes to multiple bend points, this experiment was restricted to a single bend point. The values b_{ij}, for $i = [1, m]$ and $j = [1, n]$ represent the training set of known bend points. For a single bend point, $i = 1$ and $j = 1$. The value b_{xj} represents the j^{th} bend value for an image interpolated to be between k and $k+1$, for $k = [1, m-1]$; that is $k \leq x \leq k+1$ For this experiment $m = 20$.

The neural network was trained with few epochs. For a simple 76800, 100, 10, 1 layer neural network, just under 40 epoch would give reasonable results, but with more severe binning. The graph in figure 4.5 shows the fit for 600 unseen speckle images. The training set are the green points and the unseen images are the red points. The number of epochs to train this 76800, 500, 100, 1 layer neural network was 268.

4.1.3 Results

A simple neural network consisting of 4 layers was sufficient to store a small image database that encoded the shape information of the fiber optic cable. Twenty images was sufficient to give good results. Starting with 10 output neurons or clusters, the results were pretty good. Using 20, or even 100, gave better results. Using raw, input images, scaled to 1/2 or 1/4 of their original size, the neural network could be trained reasonably well, but, if a Gaussian blur (5x5) is applied, then the training times improve and the results are more consistent. Basically, increasing the signal-to-noise ratio (SNR) reduces the error of the neural network. For a discussion of evaluating modal noise see [53]. Noise is not a concern, except that it impacts the neural network training time. The neural network provided a direct readout of the fiber displacement for one bend location, however, extending the system to calibrate and measure multiple bend points is extremely difficult; mathematically, a very complex problem.

4.2 Experiment 2 - MEMS accelerometer error analysis

The MEMS accelerometer – the iPod® – is the device used to provide the output training set and to validate the fiber accelerometer performance. This section describes the two experiments to analyze the error of the iPod® accelerometer. It cannot be expected that any two accelerometers are exactly the same, despite how carefully they are constructed. Nor, can it be expected that the accelerometer sensors

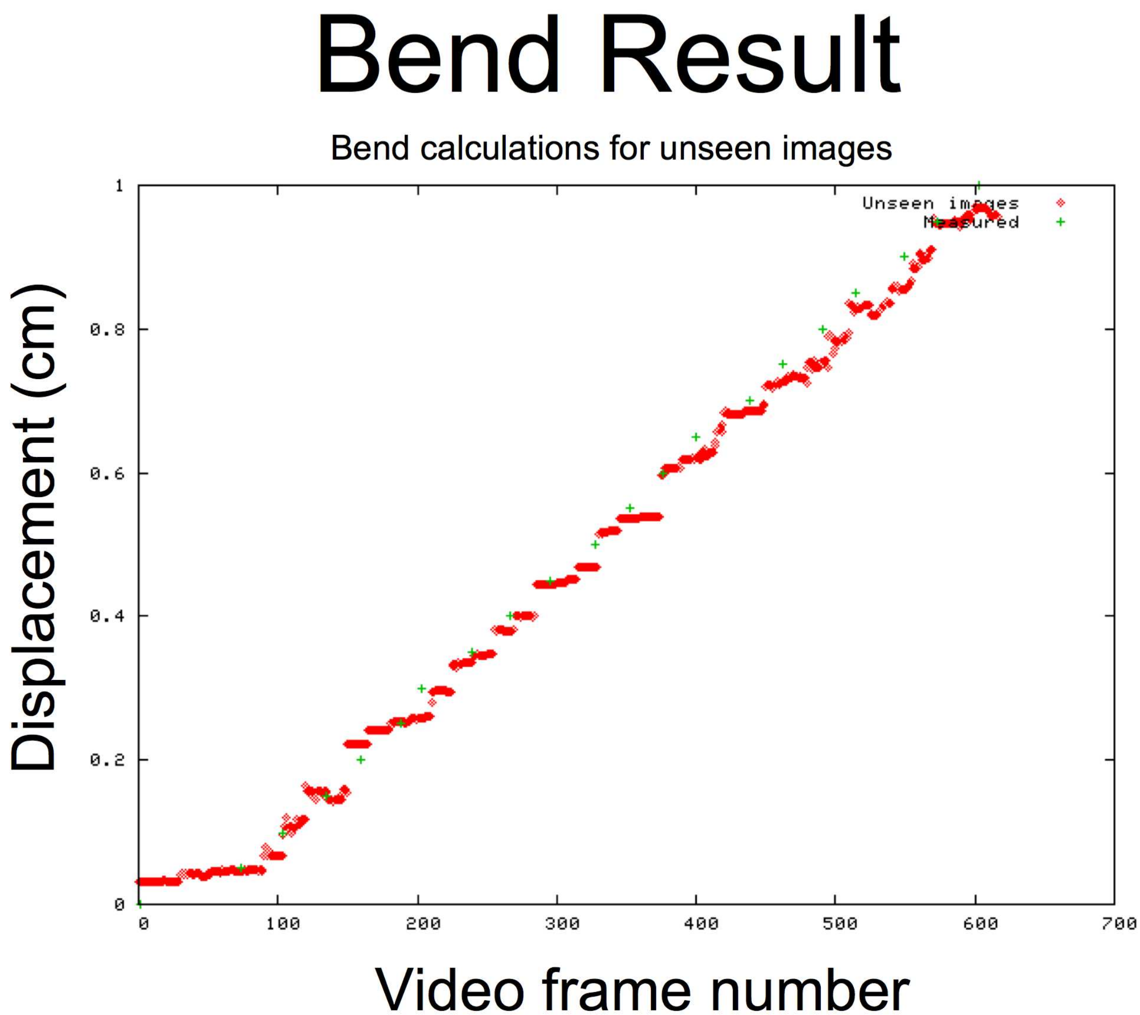

Figure 4.5: Graph of the single bend results. The training set of 20 images is shown in green. The execution on the remaining 600 images is shown in red. Ideally, all the points should lie in a straight line. The architecture of the neural network is four layers (2 hidden) consisting of 76800 input nodes (320x240 image, one node per pixel), 500 and 200 nodes for each hidden layer, and one output node. This network required 268 training epochs to converge with an error < 0.0002.

are mounted exactly the same way within the iPod. Experiment 2 illustrates that these considerations must be taken into account when calibrating and validating the fiber accelerometer.

A custom iPod application was written to collect accelerometer data and store it as a file on the iPod. That file is transferred to a computer, using the iTunes interface, for analysis.

4.2.1 Setup and data collection

The iPods® are compared while they are stationary. The goal is to measure the differences between the iPods® and obtain statistics, for the error this sensor exhibits, in order to construct a confidence interval for comparison – the iPod® accelerometer is being used to calibrate and validate the fiber accelerometer. The experimental steps are:

- Two iPods are placed next to each other and on the vibration isolated table.
- The acceleration application is started.
- It is run for about 30 seconds.
- The application is stopped.
- The data is transferred to a computer for analysis using the iTunes interface.
- The magnitude of the sum of all three axes is computed and plotted.

4.2.2 Results

Figure 4.6 shows the data obtained from two iPod's®. The vertical separation indicates the difference between two accelerometers on each iPod®. Nominally, each accelerometer should maintain a value of 1 when stationary; that is 1 g – the force of gravity is always present even for stationary objects. The statistics for each iPod®, where n is the number of samples, is:

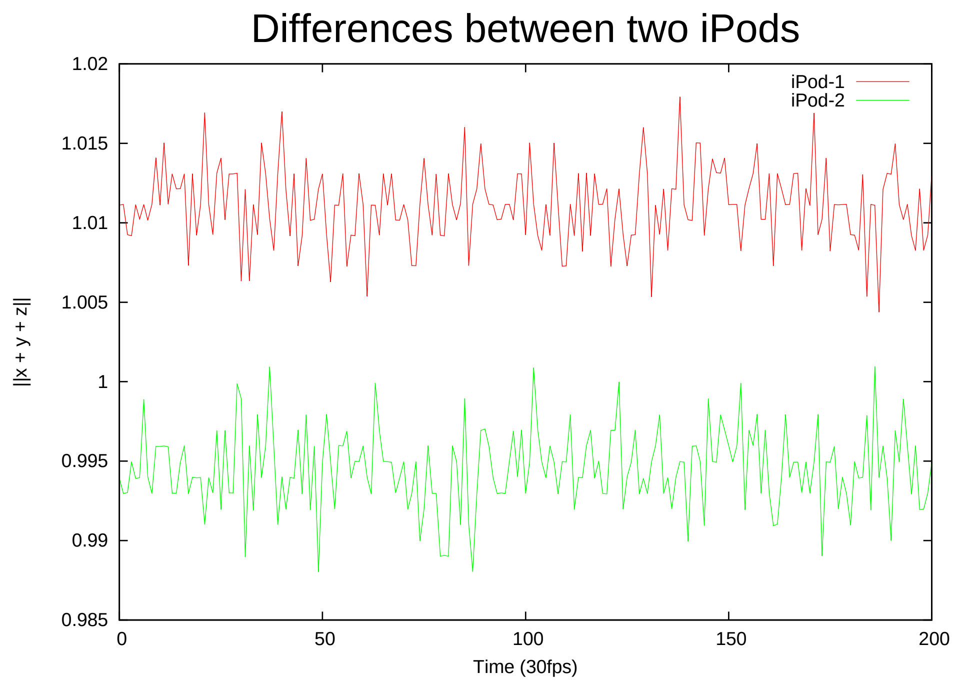

Figure 4.6: Accelerometer differences between two iPods® while sitting stationary on a vibration isolated table. A perfect accelerometer would measure 1g, however the iPods® have inexpensive MEMS accelerometers which are noisy and not mounted perfectly within the case. The mean and standard deviation are used in the analysis to construct a confidence interval when comparing it to the fiber accelerometer.

- iPod - 1: $\mu = 1.0111, \sigma = 0.00238$, for $n = 1023$.
- iPod - 2: $\mu = 0.995, \sigma = 0.00244$, for $n = 1024$.

That is when all three axes are combined. However, for the pendulum experiment (see section 4.4), only one axis is going to be used; the x-axis of the iPod® accelerometer. Plotting the x-axis accelerometer differences is shown in figure 4.7. The mean and standard deviation of that axis will be used to determine the confidence interval when comparing the fiber accelerometer data with the iPod® acceleration data. One factor contributing to the mean differences between the two accelerometers is their physical orientation. That orientation may not be perfectly aligned with the iPod® case; and varies from iPod® to iPod®. For a perfectly mounted accelerometer in an iPod® lying on a level surface, $\mu_x = 0$. The angle offset for the sensor mount – from level – is $sin^{-1}(\mu_x)$; similarly, for μ_y and μ_z.

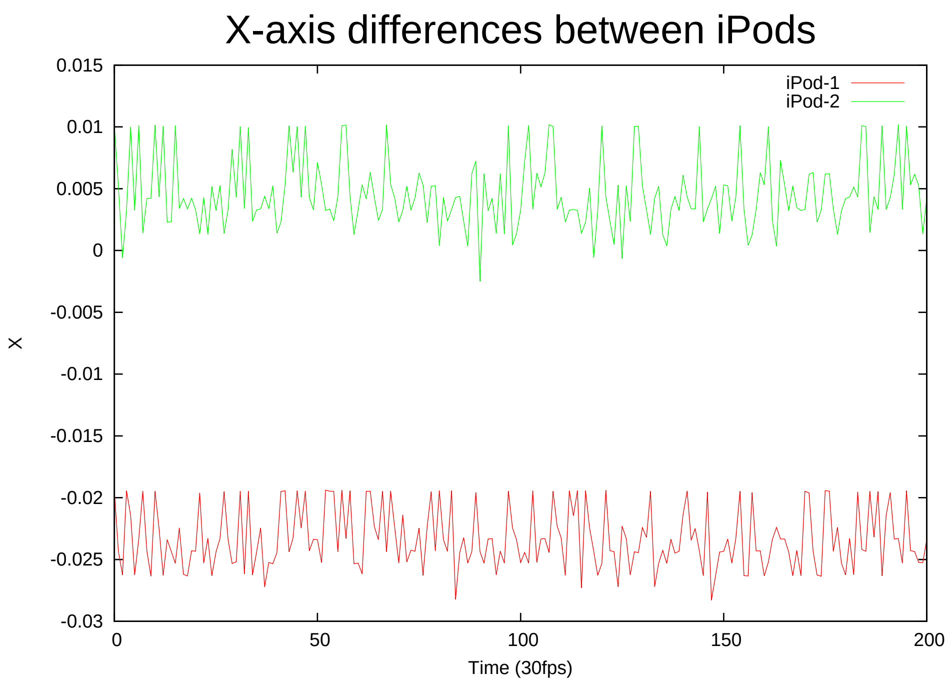

Figure 4.7: The X-axis accelerometer differences between two iPods® while sitting stationary on a vibration isolated table. Ideally, the reading should be 0. Noise, likely due to electromagnetic radiation from the circuit board, must be considered. It is the x-axis accelerometer data that will be collected for validation with the fiber accelerometer.

The statistics for each iPod® is:

- iPod - 1: $\mu_x = -0.023, \sigma_x = 0.00262$.
- iPod - 2: $\mu_x = 0.004, \sigma_x = 0.00273$.

4.3 Experiment 3 - Fiber light transfers

Proof-of-concept is sufficient because the actual manufacturing of this device at the scales needed are beyond the scope of this dissertation. However, it is necessary to show that sufficient light is captured across an “air-gap” to prove that it is technically possible with current technologies.

4.3.1 Air-gap I and II

The first experiment demonstrates that light from a multimode fiber can be transferred to a single-mode fiber over an air gap. It is not necessary that the light transfer be efficient, since detection of light is the only requirement. A schematic of the experiment is illustrated in figure 4.8a. The second demonstration is light being transferred to another fiber after it has been reflected by a mirror. A schematic of that experiment is illustrated in figure 4.8b.

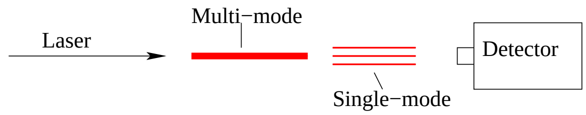

(a) Detecting light from a multi-mode to a single-mode, over an air gap, without any lenses to focus the light.

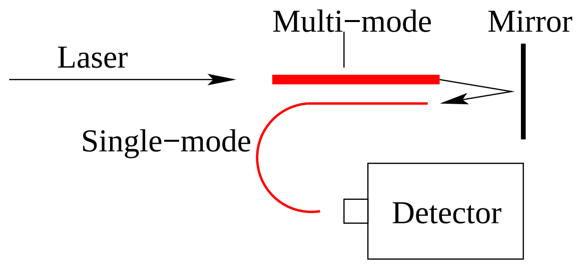

(b) Detecting light from a multi-mode to a single-mode after reflecting it from a mirror, without any lenses to focus the light.

Figure 4.8: Air-gap experiments.

4.3.2 Setup and data collection

The source fiber is mounted in a rigid mount. The target fibers are mounted using modeling clay. A microscope camera is utilized for the detector, however a standard handheld camera is also used. Figure 4.9 shows the experimental setup. The target fibers are mounted on modeling clay supports.

4.3.3 Results

Figure 4.10a is a single frame from the video capture showing two red spots near the upper left. Those two red spots are the light emitted from the single-mode fiber demonstrating that the light is transferred from a single multimode fiber across an air-gap to two (could be more) single-mode fibers. Furthermore, as the multimode fiber is bent, the amount of light coming through the single-mode fibers changes. That indicates that the speckle-gram pattern changes are detectable. Similarly, figure 4.10b is a single frame from the video capture showing a single red spot; it is very tiny – located just to the right of center midway up the image. It is a demonstration that light is captured after reflecting from a mirror. The laboratory setup is very inefficient

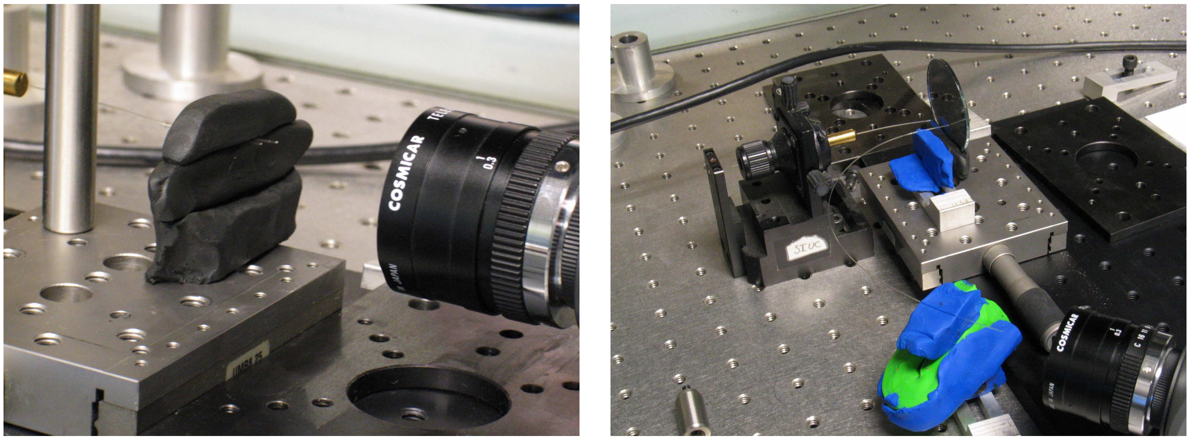

(a) (b)

Figure 4.9: Experimental setup for multi-mode to single-mode light transfer through the air without using a focusing lens. Two fibers are mounted with black modeling clay (a). The setup for a light transfer from a multi-mode fiber to a single-mode fiber after reflecting the light off a mirror (b). Note, the single-mode fiber is resting on top of the blue modeling clay.

and a great deal of light energy is lost, however, coupling a mirror at the end of a fiber is common practice; and, little to no light energy is lost. This demonstration is necessary to confirm that a mass-spring fiber accelerometer using a mirror after light passes through an air-gap, shown in figure 3.3, is practical and achievable.

4.4 Experiment 4 - Fiber accelerometer

This section describes the apparatus construction, the data collection and the analysis to determine the performance of the fiber accelerometer prototype. The analysis is performed as described in section 3.2. The data from the specklegram video, as the pendulum swings, is carefully synchronized with the accelerometer readings from the iPod®. Once the data is collected, it is processed through numerous stages and converted to an appropriate format for analysis.

4.4.1 Setup and data collection

The pendulum apparatus is shown in figure 4.11b. Briefly, it consists of:

- An apparatus to attach the pendulum. This is a wooden frame that is attached

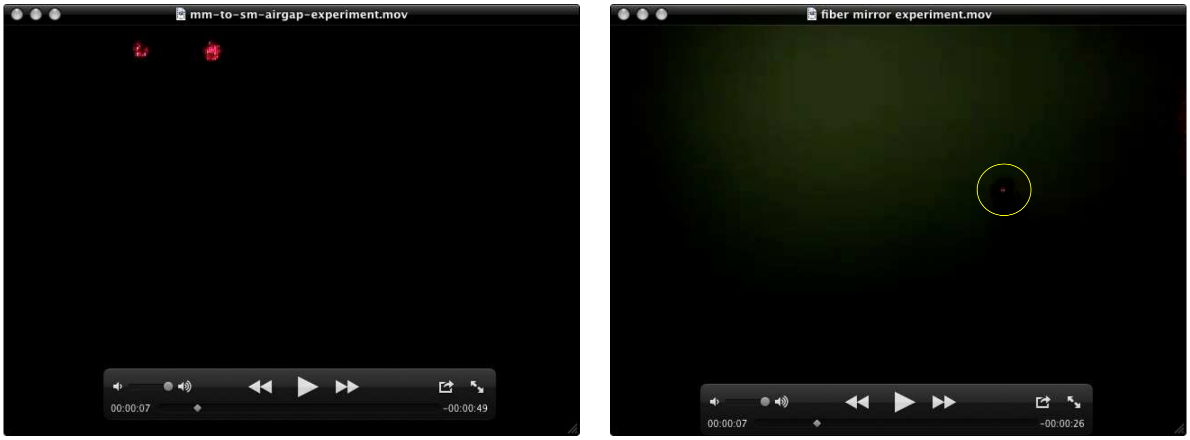

(a) (b)

Figure 4.10: Detecting the light from multi-mode to single-mode light transfer through the air without using a focusing lens, the light is transferred to two single-mode fibers (a). And, detecting the light transfer from a multi-mode fiber to a single-mode fiber after reflecting the light off a mirror. It is a very small red dot to the right of center and mid-way up in (b); inside the yellow circle.

to a vibration isolated table.

- A seven inch plastic and rubber wheel with a metal bearing.
- One meter of 1” square aluminum tubing.
- One oak board, 1”x4”x36”. This is the mounting platform for the laser, fiber and camera.
- One 90° bracket to support the iPod® (accelerometer).
- Counter weights.

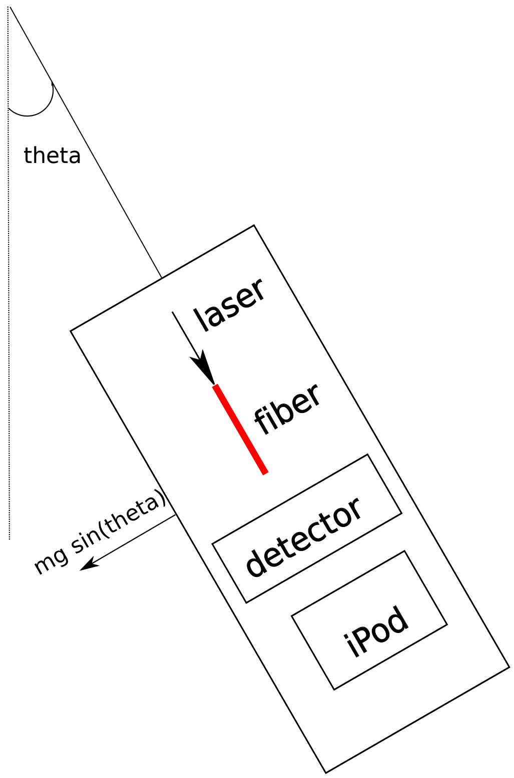

(a) Schematic

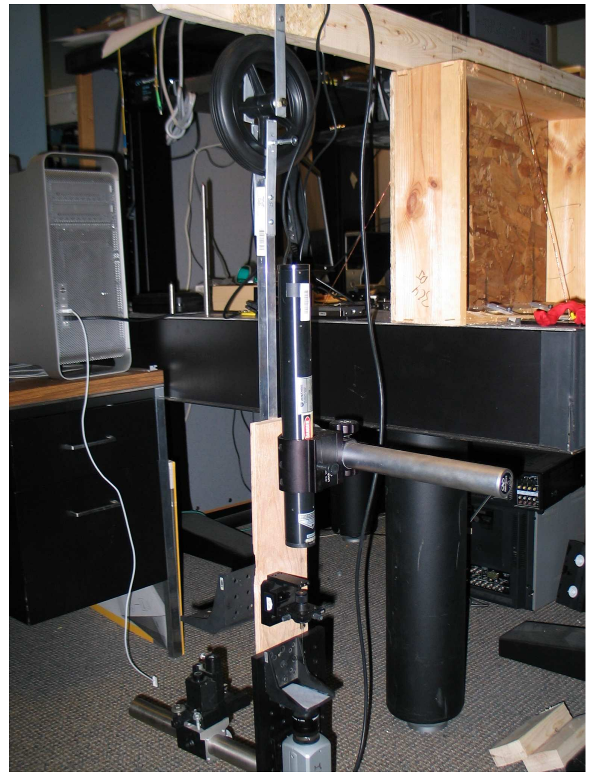

(b) Physical

Figure 4.11: The schematic of the pendulum experiment (a) shows the laser entering the multi-mode fiber and shining upon the detector, and shows the co-location of the MEMS (iPod®) accelerometer. The physical pendulum apparatus (b) is attached to frame sitting upon the vibration isolating table – to isolate it from building vibrations. The laser shines downward into a 4 inch multi-mode fiber segment with one free end. The speckle pattern is projected onto a tracing paper screen and viewed with a microscope video camera. Large counter weights are present to keep the apparatus vertical, however they add a semi-periodic rotational torque vibration when the pendulum swings; the wheel helps minimize that effect.

It is necessary that the apparatus, and thus the pendulum, be attached to the surface of the vibration isolated table. Excessive building vibration due to the large heating and air conditioning devices in the attic of the building, causes the fiber cable to vibrate which results in the ever moving and shaking speckle pattern. A sturdy wheel provides for a smooth pendulum operation, however it does not eliminate non-planar torque altogether. The setup is adequate for this analysis; the pendulum oscillations are nearly confined to a single plane.

The data is collected from two video camera, one accelerometer all the while the pendulum is swinging. Custom software was written to:

- perform real-time multiple camera capture.
- collect real-time accelerometer data from an iPod®. The set of points for the iPod® is: $P : \{(x, y)_j : j \in \{1..p\}\}$
- determine synchronization points for the accelerometer data and the speckle patterns.

The pendulum is set into motion, then the camera capture begins. Once the desired swing amplitude is obtained, the iPod® application is started; one camera records that moment. About 40 seconds of data are collected per experiment.

- Place laser (led light), focusing lens, mm fiber, camera on a fixed platform.
- Suspend downward to create a pendulum.
- Swing the pendulum.
- The set of points for the fiber is, $F : \{(x, y)_i : i \in \{1..n\}\}$

Here is the basic algorithm for performing the analysis:

- Smooth the accelerometer data.
- Compute statistics for the accelerometer data. This repeats experiment 4.2. The operation of the pendulum may introduce more error in the x-axis accelerometer measurements. A full analysis, to determine if that is actually the case, was not performed.
- Convert the speckle-gram video into a gray-scale and blurred version.
- Determine the neural network training data set. The training set will consist of speckle image for one full (the first) pendulum oscillation.

- Map the accelerometer data to the speckle-gram video frames. The MEMS accelerometer data rate is 30 measurements per second. That matches the video camera frame rate. The MEMS accelerometer data is matched to the speckle-gram video using a second video camera to record the exact moment that the MEMS accelerometer begins collecting data.

- Determine the neural network architecture. The same neural network architecture used in the single bend experiment in section 4.1 is used. It is a feed-forward back-propagation four layer (two hidden) neural network with 76800, 500, 200, 1 nodes per layer (from input to output).

- Train the neural network.

- Run the entire speckle-gram video through the trained neural network.

- Compute the differences between the output of the neural network run and the accelerometer data, using the technique described in section 3.4.

- Plot the differences.

4.4.2 Results

The confidence interval is calculated based on the statistical error for the iPod® accelerometer. In this case, the accelerometer data is smoothed using an averaging window of size 5. Then, the difference from this smoothed data to the accelerometer data is calculated to obtain the means and standard deviation. This is used to compute the confidence interval for comparing data to the iPod® accelerometer. Table 4.1 shows the confidence intervals. To interpret the confidence interval, you say, “The two curves are different, with a 99.9% confidence level, when the mean difference is greater than 0.00246.” It is not appropriate to say, “The two curves match when the mean difference is less than 0.00246.” However, for this study, when the curves are not different, then indications are that they are the same; but, there is no confidence value assigned to that statement.

Table 4.1: Confidence intervals for the MEMS accelerometer with $\mu = 0.002281$ and $\sigma = 0.00197$. This interval is computed by placing the device on the pendulum and computing a mean of five values. The difference between that and the raw data defines the statistics. Notice that these numbers are different from those obtained in experiment 4.2, because the device may be at a slightly different 3-space orientation; it affects all accelerometer axes.

Confidence Interval (%)	min	max
50	0	0.002317
60	0	0.002326
70	0	0.002337
80	0	0.002350
90	0	0.002369
95	0	0.002386
98	0	0.002406
99	0	0.002419
99.9	0	0.002460

The mean difference between the fiber accelerometer data and the iPod® accelerometer data, for two time ranges, is shown in table 4.2. For the time interval $[0, 300]$ – the first 300 measurements, the mean difference is within the 99.9% confidence interval; so one can say, “Since the mean difference lies within the 99.9% confidence interval, there is no significant difference between the two datasets for the time range $[0, 300]$.” For the second time interval, $[0, 400]$, one can say, “However, for the time range $[0, 400]$ we are 99.9% confident that there is a significant difference between the two curves; therefore, they are different over that time interval.”

Table 4.2: Comparison of the fiber and MEMS accelerometers.

Frame range	μ	σ	Do the curves match?
0 to 300	0.00222	0.00215	Yes.
0 to 400	0.00268	0.00282	No.

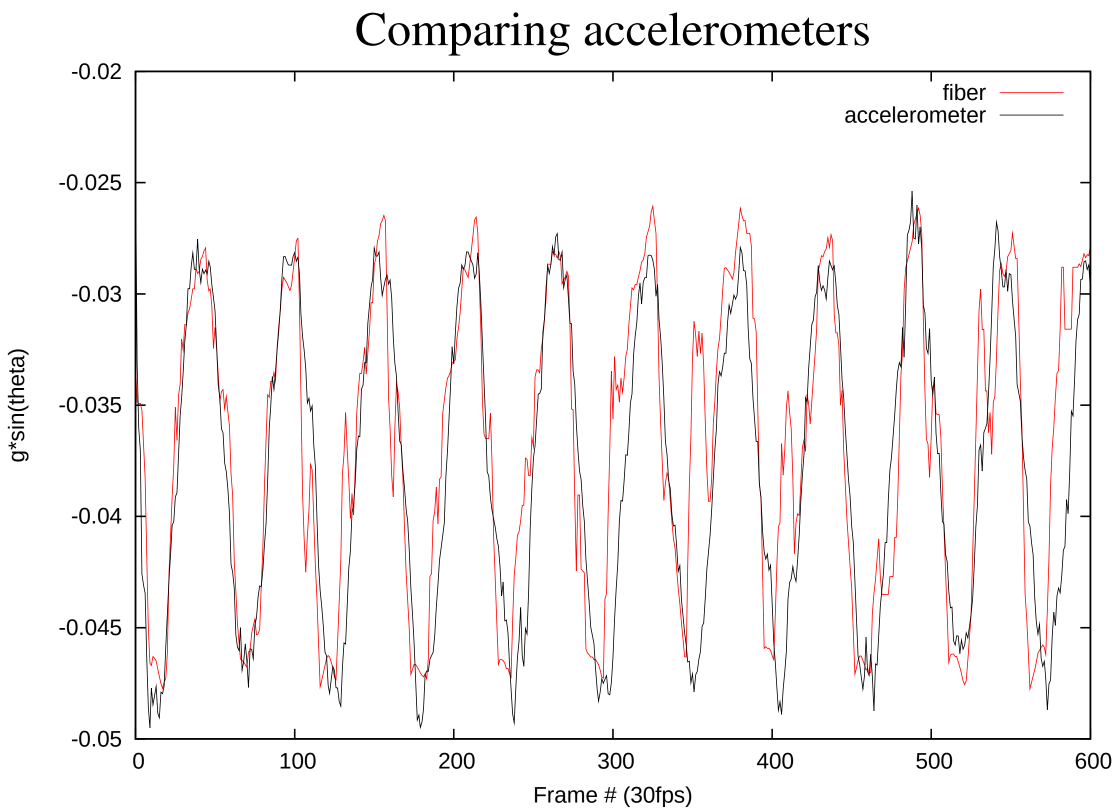

Figure 4.12: This graph shows the fiber accelerometer (red) plotted with the validation accelerometer (black); a feed-forward back-propagation neural network with 76800, 500, 200, 1 layers. This neural network required approximately 1000 training epochs. For the first 300 frames (10 seconds), the performance of the fiber accelerometer is indistinguishable from the MEMS accelerometer. However, from 0 to 400 there is a significant difference; notice the deviation between frames 300 and 450. The most likely cause is the large counter balance weights producing a torque vibration (possibly periodic).

CHAPTER 5: DISCUSSION

This dissertation study presents a novel positional sensor for 3D vascular reconstruction – in the context of cardiovascular research, diagnostics and treatment, to track a catheter in vivo – and provides examples of experimentation illustrating its feasibility of construction, calibration and validation.

Four experiments were carried out to test different aspects of the fiber accelerometer architecture illustrated in figure 5.1. Experiment 4, in section 4.4, tests that the magnitude of a single bend, in the sensor, caused by motion of the “mass-spring”, is computable. Non-linear processing tracks the magnitude of the bend precisely. Experiment 2, on page 46, tests that light can be transferred over an “air-gap” to single-mode fibers. This is necessary to determine the direction of motion vector. Experiment 3, on page 51, illustrates the error with a MEMS accelerometer. Finally, experiment 4, on page 53, operates the fiber accelerometer in a single plane of motion. Non-linear processing is able match the MEMS accelerometer readings. The setup for experiment 4 does not represent the “in vivo” setup accurately and the non-linear processing is computing two numbers from the speckle-gram[1]:

1. The magnitude of the bend.
2. The direction of the bend.

While item 1 is part of the architectural design, item 2 is not. Experiment 4 must be modified to fix the end of the fiber such that the motion of the fiber tip is stationary relative to the detector (the camera). This would be the effect if a mirror were to reflect the light back through the fiber for detection at some point before the tip (the

[1] The careful reader will notice that the non-linear processing is integrating much more: longitudinal force ($mg\,cos(\theta)$), inertia, gravity (mg), and pendulum tension, etc.

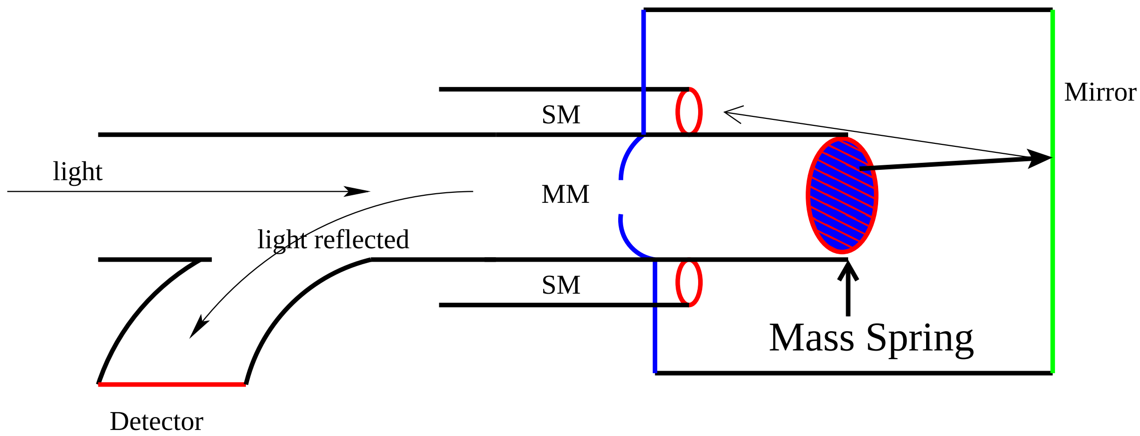

Figure 5.1: The fiber, in vivo, architecture. Shown as bare fibers, the “mass-spring” is a heavy one-way, or two-way, mirror (indicated by the red/blue pattern).

location of the mass-spring), see figure 5.1. Experiment 1, in section 4.1, has shown that the analysis of a single bend, somewhere before the end of the fiber, is able to compute the magnitude of the bend. Then, to determine the direction of the bend, the techniques described in experiment 2, in section 4.2, would be employed.

This research is original because a neural network has not been applied to a fiber accelerometer wherein the multi-mode speckle-gram is analyzed for quantitative comparison with a traditional accelerometer.

This research is novel because traditional accelerometers are bulky and, as such, have not been considered to be appropriate devices for in vivo catheter applications. A fiber accelerometer, of the type presented herein, is small and eminently practical for for direct tracking of catheters. It is innovative for the very same reasons – the analysis techniques utilized are well established and not new. However, it is quite possible – even desirable – that the neural network processing be substituted for something computationally faster and mathematically simpler.

The lack of 3D vascular mapping or rendering systems suggests that a device that can provide 3D positional information to facilitate the 3D reconstruction of the vascular segment from IVUS data, may fill a void and help medical professionals with diagnostics and treatment. Such additional information could eliminate delays between invasive diagnostic surgery and treatment surgery – improving a patients quality of life; emphasizing that this research is both relevant and significant. This fiber positional sensor has the potential to save lives all the while being a simple, inexpensive and fast. The experimental results, presented herein, should be taken as proof that this research is moving in the right direction; toward a novel positional sensor for 3D vascular reconstruction.

5.1 Experimental observations

Some notable observations, from the laboratory setup, further our expectation that the multi-mode fiber accelerometer has potential as a highly sensitive and accurate device:

1. The iPod accelerometer data is very noisy. This is typical of MEMS accelerometers that are not highly sensitive. However, the fiber speckle-gram did not fluctuate and remained stable and stationary. This would suggest that this type of fiber accelerometer would provide "very clean" acceleration measurements; that the signal to noise (SNR) is much higher for the fiber accelerometer.

2. The fiber accelerometer was tested in only one plane of motion, however, the experimental setup and design generalize to the other two spatial planes. The apparatus for the experimentation would be more elaborate and the data collection for verification more complex, but the experiment is eminently practical.

3. Initially, the pendulum apparatus was attached to the frame of the table. The frame is not vibration isolated from the building. The heating and cooling machinery located in the attic of the building shook the room, where the experiments were conducted, such that it caused visible vibrations in the speckle-gram. This vibrational noise was intolerable and impossible to compensate for during analysis. The remedy was to attach the pendulum to the surface of the

vibration isolated table. Once that was done, the speckle-gram was absolutely stable with excellent results forthwith.

4. Refinements in the pendulum apparatus construction may eliminate some sources of error and excess noise. For instance, the fiber is exposed and subject to air currents and minimal lighting is required for the video capture. Enclosing the fiber and laser apparatus on the pendulum would eliminate that potential sources of noise.

5. The pendulum apparatus is very bulky and weighs nearly 30 pounds. The laser system is mounted on a very heavy structure and, for the pendulum to operate in a plane, the addition of an equally heavy counter-balance is needed. The laser mount and the counter-balance posts protrude about 15 inches. This protrusion and weight causes the pendulum to wobble and is the primary source of noise during the data collection. Using laser diodes as sources of laser light would eliminate the bulky apparatus resulting in a smoother operating pendulum.

5.2 Looking ahead

This study opens the door for further research and development toward a multi-mode fiber accelerometer. The multimode fiber accelerometer is sensitive enough to measure the vibration of Woodward Hall, located at the University of North Carolina at Charlotte. It is a four story steel I-Beam framed brick building and the vibration is due to the operation of the heating and cooling machinery located in the attic. To eliminate the vibration from interfering with the experimental setup, the pendulum apparatus was placed on a vibration isolated table; just a few years earlier, the most sensitive MEMS accelerometer was announced[35]. The question begs itself, "how would the multi-mode fiber accelerometer, if constructed using MEMS technology, fair by comparison?"

BIBLIOGRAPHY

[1] "The Impact of Stent Deployment Techniques on Clinical Outcomes of Patient Treated With the CYPHER® Stent (S.T.L.L.R.)." http://clinicaltrials.gov/ct/show/NCT00403338. Cordis Corporation. Study completed April 2006.

[2] K. Shojania, B. Duncan, K. McDonald, R. Wachter, and A. Markowitz, *Making health care safer: a critical analysis of patient safety practices*. Agency for Healthcare Research and Quality Rockville, MD, 2001.

[3] K. Subramanian, M. Thubrikar, B. Fowler, M. Mostafavi, and M. Funk, "Accurate 3D reconstruction of complex blood vessel geometries from intravascular ultrasound images: in vitro study," *Journal of Medical Engineering & Technology*, vol. 24, no. 4, pp. 131–140, 2000.

[4] S. Solomon, T. Dickfeld, and H. Calkins, "Real-Time Cardiac Catheter Navigation on Three-Dimensional CT Images," *Journal of Interventional Cardiac Electrophysiology*, vol. 8, no. 1, pp. 27–36, 2003.

[5] M. Schneider and C. Stevens, "Development and testing of a new magnetic-tracking device for image guidance," in *Proceedings of SPIE medical imaging*, pp. 17–22, 2007.

[6] M. Heron, D. Hoyert, J. Xu, S. Chester, and B. Tejada-Vera, "Deaths: Preliminary data for 2006," *US Dept of Health and Human Services - National Vital Statistics Report*, vol. 56, June 2008.

[7] J. Xu, K. Kochanek, S. Murphy, and B. Tejada-Vera, "Deaths: Final data for 2007," *US Dept of Health and Human Services - National Vital Statistics Reports*, vol. 58, May 2010.

[8] S. Nissen, "IVUS is redefining atherosclerotic disease.," *Circulation*, vol. 103, pp. 2705–2710, 2001.

[9] J. Noble and D. Boukerroui, "Ultrasound image segmentation: A survey," *IEEE Transactions on medical imaging*, vol. 25, no. 8, pp. 987–1010, 2006.

[10] T. Binder, "Three-Dimensional Echocardiography-Principles and Promises," *Journal of Clinical and Basic Cardiology*, vol. 5, no. 2, pp. 149–152, 2002.

[11] C. Kirbas and F. Quek, "A review of vessel extraction techniques and algorithms," *ACM Computing Surveys*, vol. 36, no. 2, pp. 81–121, 2004.

[12] "Cardiop-B<AE>." Registered trademark by Paieon Inc.

[13] "iLab® Ultrasound Imaging System." Boston Scientific.

[14] "Eagle Eye®," 2010. Volcano Corporation.

[15] A. Wahle, G. Prause, S. DeJong, and M. Sonka, "Geometrically correct 3-D reconstruction of intravascularultrasound images by fusion with biplane angiography-methods andvalidation," *Medical Imaging, IEEE Transactions on*, vol. 18, no. 8, pp. 686–699, 1999.

[16] A. Glowinski, G. Adam, A. Bucker, J. Neuerburg, J. van Vaals, and R. Gunther, "Catheter visualization using locally induced, actively controlled field inhomogeneities.," *Magn Reson Med*, vol. 38, no. 2, pp. 253–8, 1997.

[17] M. Konings, L. Bartels, C. van Swol, and C. Bakker, "Development of an MR-safe tracking catheter with a laser-driven tip coil," *Journal of Magnetic Resonance Imaging*, vol. 13, no. 1, pp. 131–135, 2001.

[18] R. Martin, R. Hatangadi, and G. Bashein, "Method and apparatus for three-dimensional translumenal ultrasonic imaging," Mar. 21 1995. US Patent 5,398,691.

[19] M. Schneider and C. Stevens, "Development and testing of a new magnetic-tracking device for image guidance," *Proceedings of SPIE*, vol. 6509, p. 65090I, 2007.

[20] M. Rosales, P. Radeva, O. Rodriguez-Leor, and D. Gil, "Modelling of image-catheter motion for 3-D IVUS," *Medical Image Analysis*, vol. 13, no. 1, pp. 91–104, 2009.

[21] K. Rhode, D. Hill, P. Edwards, J. Hipwell, D. Rueckert, G. Sanchez-Ortiz, S. Hegde, V. Rahunathan, and R. Razavi, "Registration and tracking to integrate X-ray and MR images in an XMR Facility," *Medical Imaging, IEEE Transactions on*, vol. 22, no. 11, pp. 1369–1378, 2003.

[22] R. Jain, R. Kasturi, and B. Schunck, *Machine vision*. McGraw-Hill, 1995.

[23] R. Tsai, "An efficient and accurate camera calibration technique for 3D machine vision," in *Proceedings of IEEE Conference on Computer Vision and Pattern Recognition*, vol. 1, pp. 364–374, Miami Beach: IEEE Press, 1986.

[24] J. Hecht, *City of light: the story of fiber optics*. Oxford University Press, USA, 2004.

[25] H. Griffiths, K. Tong, and Y. Yang, "Honoring Charles Kuen Kao, 2009 Nobel Laureate in Physics," *IEEE Communications Magazine*, p. S21, 2010.

[26] J. C. Palais, *"Fiber Optic Communication," 4th Edition*, p. 30. Upper Saddle River, New Jersey: Prentice Hall, 1984.

[27] J. C. Palais, *"Fiber Optic Communication," 4th Edition*, p. 46. Upper Saddle River, New Jersey: Prentice Hall, 1984.

[28] J. C. Palais, *"Fiber Optic Communication," 4th Edition*, p. 45. Upper Saddle River, New Jersey: Prentice Hall, 1984.

[29] J. C. Palais, *"Fiber Optic Communication," 4th Edition*, pp. 116–117. Upper Saddle River, New Jersey: Prentice Hall, 1984.

[30] K. Iizuka, *Elements of photonics*. Wiley and Sons, New York, 2002.

[31] T. Gangopadhyay, M. Majumder, A. Kumar Chakraborty, A. Kumar Dikshit, and D. Kumar Bhattacharya, "Fibre Bragg Grating strain sensor and study of its packaging material for use in critical analysis on steel structure," *Sensors and Actuators A: Physical*, vol. 150, no. 1, pp. 78–86, 2009.

[32] "http://en.wikipedia.org/wiki/Fiber_Bragg_grating."

[33] R. Marusarz and M. Sayeh, "Neural network-based multimode fiber-optic information transmission," *Applied Optics*, vol. 40, no. 2, pp. 219–227, 2001.

[34] M. Sayeh, R. Viswanathan, and S. Dhali, "Neural networks for smart structures with fiber optic sensors," in *Proceedings of SPIE*, vol. 1396, p. 417, 1991.

[35] R. Waters and M. Aklufi, "Micro-electro-mechanical systems ultra-sensitive accelerometer," June 24 2003. US Patent 6,581,465.

[36] J. Kalenik and R. Pajak, "A cantilever optical-fiber accelerometer," *Sensors and Actuators A: Physical*, vol. 68, no. 1-3, pp. 350–355, 1998.

[37] J. Freal, C. Zarobila, and C. Davis, "Optical fiber microbend horizontal accelerometer," Jan. 24 1989. US Patent 4,800,267.

[38] D. McMahon, "Multimode optical fiber accelerometer," June 17 1986. US Patent 4,595,830.

[39] C. Davis Jr and T. Giallorenzi, "Fiber optic accelerometer and method of measuring inertial force," Mar. 30 1982. US Patent 4,322,829.

[40] E. Udd, "An overview of fiber-optic sensors," *Review of Scientific Instruments*, vol. 66, no. 8, pp. 4015–4030, 2009.

[41] T.-R. Hsu, *"MEMS and Microsystems: design , manufacture, and nanoscale engineering," 2nd Edition*. Hoboken, New Jersey: John Wiley & Sons, Inc., 2008.

[42] A. Gerges, T. Newson, J. Jones, and D. Jackson, "High-sensitivity fiber-optic accelerometer," *Optics letters*, vol. 14, no. 4, pp. 251–253, 1989.

[43] T. Gangopadhyay, "Prospects for fibre Bragg gratings and Fabry-Perot interferometers in fibre-optic vibration sensing," *Sensors and Actuators A: Physical*, vol. 113, no. 1, pp. 20–38, 2004.

[44] Z. Lunwei, Q. Jinwu, S. Linyong, and Z. Yanan, "FBG sensor devices for spatial shape detection of intelligent colonoscope," *Robotics and Automation, 2004. Proceedings. ICRA'04. 2004 IEEE International Conference on*, vol. 1, 2004.

[45] T. Allsop, M. Dubov, A. Martinez, F. Floreani, I. Khrushchev, D. Webb, and I. Bennion, "Long period grating directional bend sensor based on asymmetric index modification of cladding," *Electronics Letters*, vol. 41, no. 2, pp. 59–60, 2005.

[46] Y. Wang and Y. Rao, "A novel long period fiber grating sensor measuring curvature and determining bend-direction simultaneously," *Sensors Journal, IEEE*, vol. 5, no. 5, pp. 839–843, 2005.

[47] F. Yu and S. Yin, *Fiber Optic Sensors*. Marcel Dekker, 2002.

[48] B. Regez, M. Sayeh, M. A., and F. F., "A novel fiber optics based method to measure very low strains in large scale infrastructures," *Measurement*, 2008.

[49] J. Merritt, M. Sayeh, and M. T. Mostafavi, "Intelligent Shape Sensor," *ASPE Proceedings. ASPE '07. Dallas TX*, 2007.

[50] R. Kirk, *Experimental Design: Procedures for the behavioral sciences - Third Edition*, pp. 60–64. Belmont, CA: Brooks/Cole, 1995.

[51] R. Kirk, *Experimental Design: Procedures for the behavioral sciences - Third Edition*. Belmont, CA: Brooks/Cole, 1995.

[52] L. Fausett, *Fundamentals of neural networks: architectures, algorithms, and applications*. Prentice-Hall Englewood Cliffs, NJ, 1994.

[53] T. Kanada, "Evaluation of modal noise in multimode fiber-optic systems," *Lightwave Technology*, vol. 2, no. 1, pp. 11–18, 1984.

[54] R. Serway, *Physics for Scientists & Engineers*. Saunders College Publishing., 1982.

APPENDIX A: FIBER INTERFEROMETRY

There are six primary fiber technologies which may lead to a practical fiber shape sensor. A fiber shape sensor for colonoscopy has been demonstrated in Lunwei et al.[44]. It utilizes the Mach-Zahnder interferometer.

The pages that follow present possible experimental setups to explore using fiber cables as accelerometer and gyroscopic sensors. Each experiment illustrates an experimental setup and a product setup. The experimental setup is the architecture suitable for the setup in the lab. It differs from the product setup due to the placement of the detector as a result of using a mirror.

Polarization

Need

1. polarizer (to act as a reference – initially dark).

2. 633 nm fiber.

3. Detector (or camera).

Experimental setup

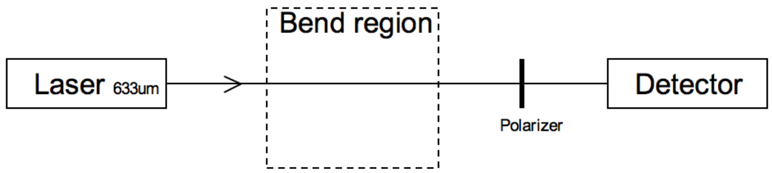

Figure A.1: Experimental setup.

Product setup

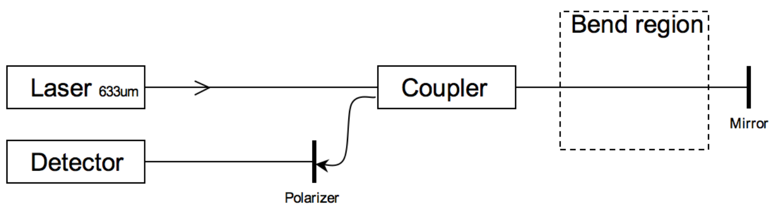

Figure A.2: Product.

Speckle pattern, SMF or MMF

At UNCC

NEED

1. Nothing.

Experimental setup

1. Use 1550 S.M.F.

2. Use 120μmmultimode fiber (MMF).

3. The detector is a CCD camera.

4. The 120μm will produce a large 2D specle pattern.

5. The 1550 SMF will produce a small speckle pattern.

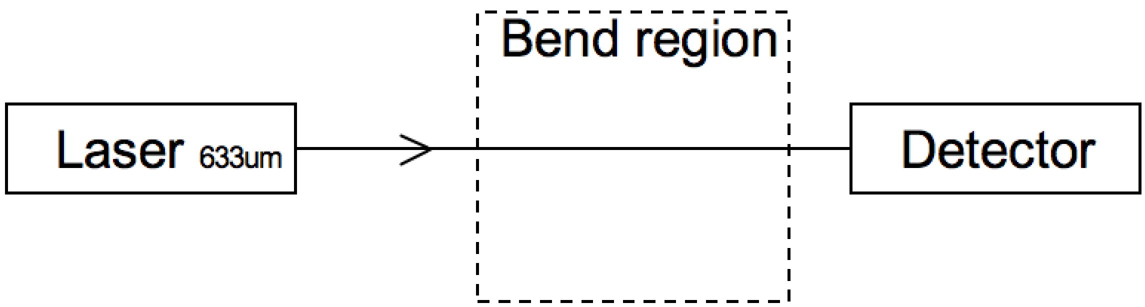

Figure A.3: Experimental setup.

Product setup

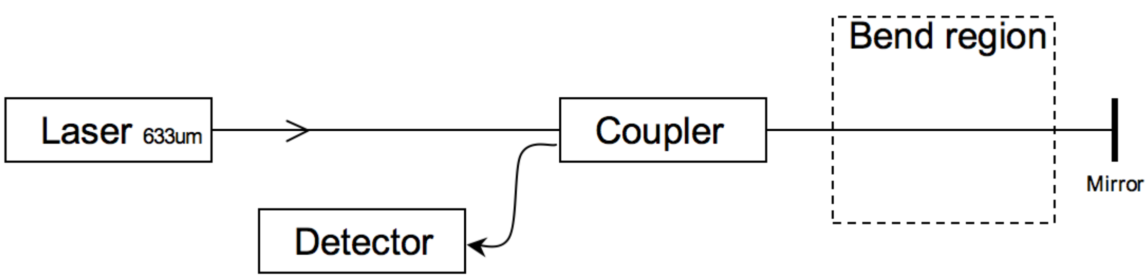

Figure A.4: Product.

Mach-Zahnder interferometer

Need

1. 2 - 1x2 or 2x2 couplers.

2. 1550 laser.

3. Detector (or camera).

Experimental setup

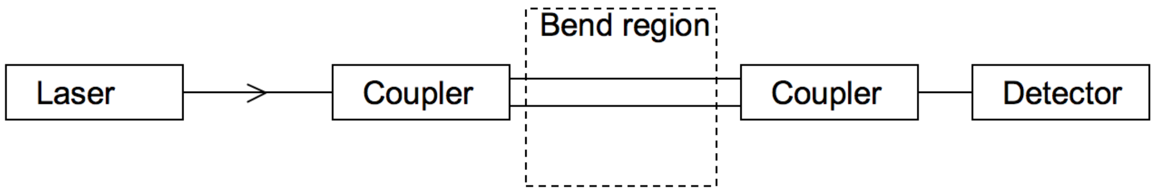

Figure A.5: Experimental setup.

Product setup

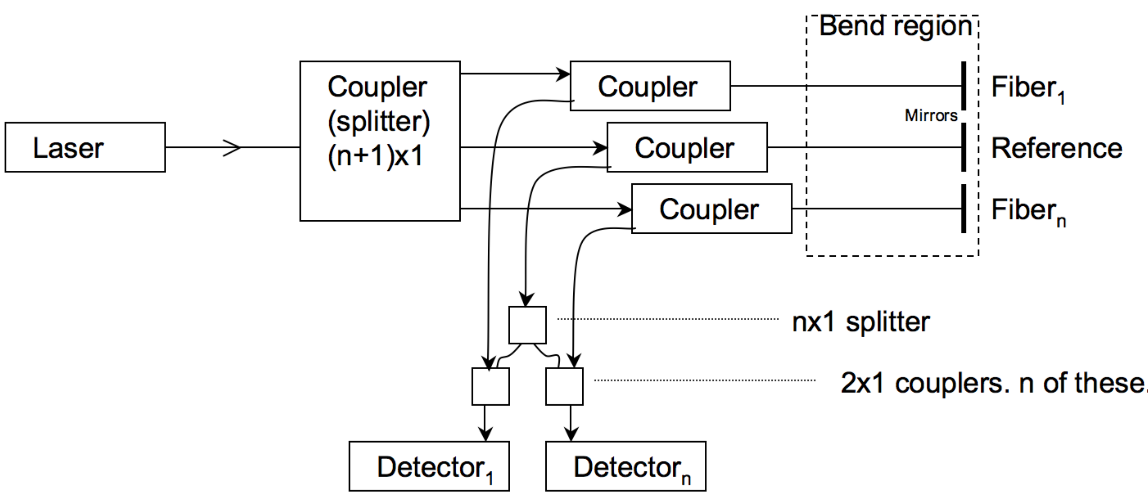

Figure A.6: Product.

Fiber Grating

At SIUC

NEED

1. Fiber grating of length d.

2. Detector is an OSA (or camera).

Experimental setup

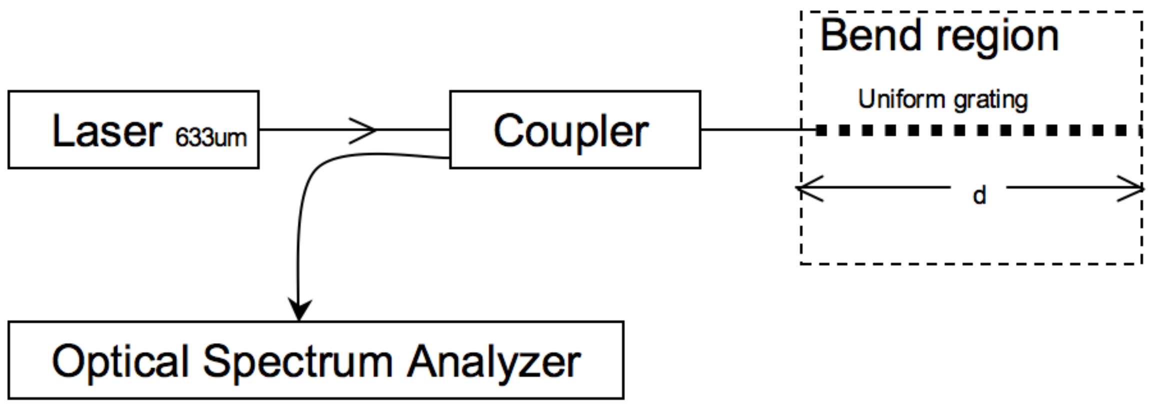

Figure A.7: Experimental setup.

Product setup

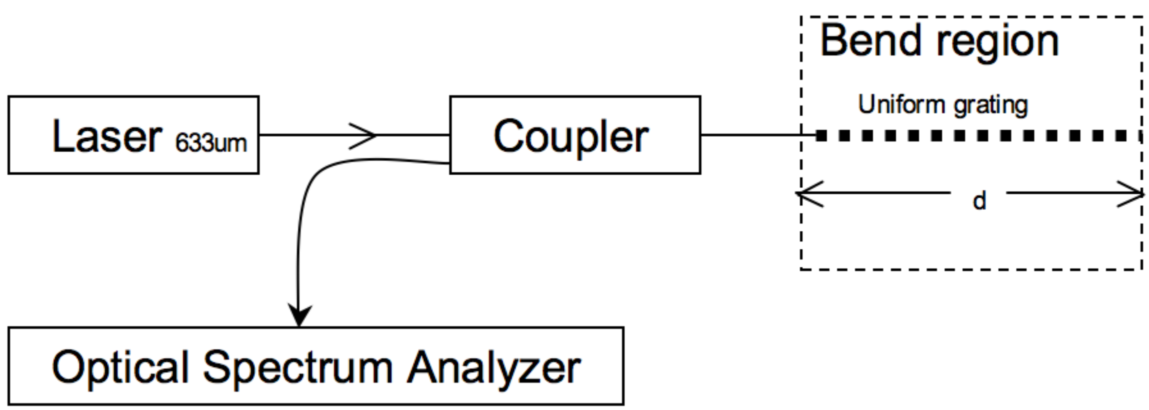

Figure A.8: Product.

Fabry-Perot resonator

At SIUC

Need

1. Fiber grating, 2 gratings spaced by d.
2. Detector is an OSA (or camera).
3. The product

Experimental setup

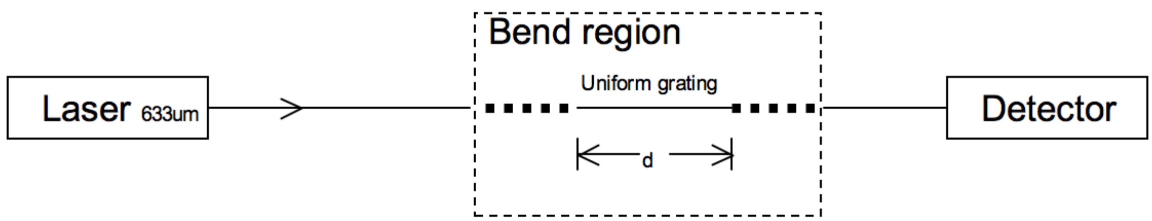

Figure A.9: Experimental setup.

Product setup

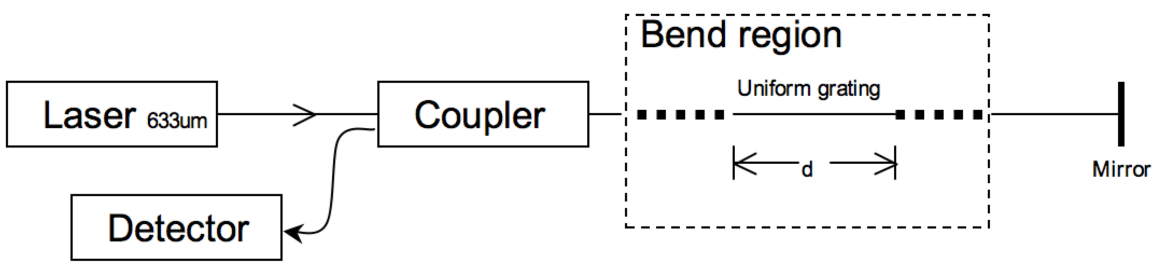

Figure A.10: Product.

Chirp grating

At SIUC

NEED

1. Chirp grating of length d.

2. Specify λ_1,λ_2,$\cdots$,λ_n.

3. The detector is an OSA.

Experimental setup

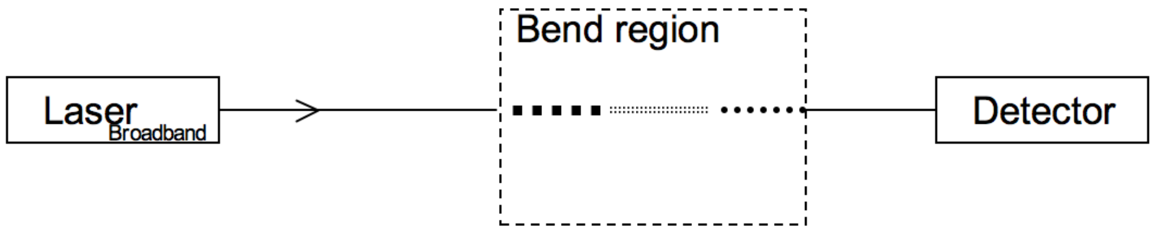

Figure A.11: Experimental setup.

Product setup

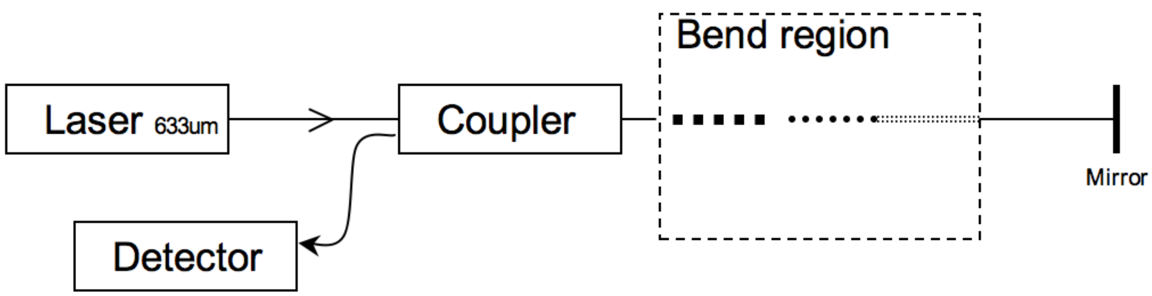

Figure A.12: Product.

APPENDIX B: STATISTICS

The statistics include herein are found in most statistical text books. Predominately, these equations come from [51].

1. Collect sample points.

2. Linear interpolate between points $y = mx + b$.

3. Repeate 1 and 2 to construct a 95% confidence interval.

$$\sigma = \sqrt{\frac{1}{n}\sum(x_i - \bar{x})^2} \tag{B.1}$$

Standard error, from the central limit theorem:

$$\frac{\sigma}{\sqrt{n}} \tag{B.2}$$

For 95% confidence, the interval is:

$$(\bar{x} - \beta, \bar{x} + \beta) \tag{B.3}$$

where

$$\beta = \frac{2\sigma}{\sqrt{n}} \tag{B.4}$$

The estimation of proportion:

$$\hat{p} = \frac{X}{n} \tag{B.5}$$

thus, the confidence interval can be written:

$$(\hat{p} - 2\sqrt{\frac{.25}{n}}, \hat{p} + 2\sqrt{\frac{.25}{n}}) = (\hat{p} - \beta), \hat{p} + \beta) \tag{B.6}$$

And the error estimate is:

$$\varepsilon \approx \beta = 2\sqrt{\frac{.25}{n}} = \frac{1}{\sqrt{n}} \tag{B.7}$$

gives

$$\frac{1}{\varepsilon^2} \approx \frac{1}{\beta^2} = n \tag{B.8}$$

Simple regression

$$y_i = \alpha + \beta x_i + \varepsilon_i \tag{B.9}$$

where

$$\alpha = \bar{y} - \hat{\beta}\bar{x} \tag{B.10}$$

and

$$\hat{\beta} = \frac{\sum x_i y_i - \frac{1}{n}\sum x_i \sum y_i}{\sum x_i^2 - \frac{1}{n}(\sum x_i)^2} \tag{B.11}$$

Co-variance

$$S_{xy} = \frac{1}{N-1}\left(\sum_{i=1}^{N} x_i y_i - \frac{\sum_{i=1}^{N} x_i \sum_{i=1}^{N} y_i}{N}\right) \tag{B.12}$$

or

$$S_{xy} = \frac{\sum_{i=1}^{N}(x_i - \overline{x})(y_i - \overline{y})}{N-1} \tag{B.13}$$

Suppose $X_1, \ldots, X_n$ are an independent sample from a normally distributed population with mean μ and variance σ^2. Let

$$\bar{X} = \frac{(X_1 + \ldots + X_n)}{n}$$

and

$$S^2 = \frac{1}{n-1}\textstyle\sum_{i=1}^{n}(X_i - \bar{X})^2$$

Then,

$$T = \frac{\bar{X} - \mu}{\frac{S}{\sqrt{n}}}$$

has a t-distribution with $n - 1$ degrees of freedom. Then, denoting c as the 95^{th} percentile of this distribution,

$$P(-c < T < c) = 0.9$$

Note: there is a 5% chance that T will be less than $-c$ and a 5% chance that it will be largere than $+c$. Thus, the probability that T will be between $-c$ and $+c$ is 90%. Consequently,

$$P(\bar{X} = \frac{cS}{\sqrt{n}} < \mu < \bar{X} + \frac{cS}{\sqrt{n}}) = 0.9$$

and we have a theoretical (stochastic) 90% confidence interval for μ. After observing the sample we find values $\bar{x}$ for $\bar{X}$ and s for S, from which we compute the confidence interval

$$\left[\bar{x} - \frac{cs}{\sqrt{n}}, \bar{x} + \frac{cs}{\sqrt{n}}\right]$$

an interval with fixed numbers as endpoints, of which we can no more say there is a certain probability it contains the parameter μ. Either μ is in this interval or isn't.

APPENDIX C: THE PENDULUM

A simple pendulum is a simple periodic oscillating mechanical system.

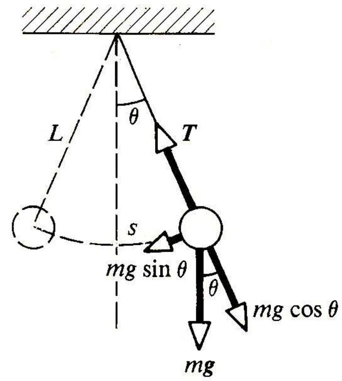

Figure C.1: A simple pendulum[54].

It consists of an object suspended by a string where the object is free to move and the other end of the string is attached to a fixed location. Its motion lies in the vertical plane and influenced by gravity. The forces acting on the object are tension, T, upward along the string and its weight, mg. Thus, the equation of motion is defined as:

$$F = ma \tag{C.1}$$

$$= -mg\, sin\theta = m\frac{d^2 s}{dt^2} \tag{C.2}$$

where s is the displacement along the arch and the minus sign indicates that F acts toward the equilibrium position. See figure C.1.

Since $s = L\theta$ and L is constant, F reduces to:

$$F = \frac{d^2\theta}{dt^2} = -\frac{g}{L} sin\theta \tag{C.3}$$

If we assume that θ is small, then $sin\theta \approx \theta$, where θ is measured in radians[1], the equation of motion becomes:

$$\frac{d^2\theta}{dt^2} = -\frac{g}{L}\theta \tag{C.4}$$

which is the equation of a simple harmonic motion: $\theta = \theta_0 cos(\omega t + \delta)$, where θ_0 is the maximum angular displacement and δ is the phase constant and the angular frequency ω is given by:

$$\omega = \sqrt{\frac{g}{L}} \tag{C.5}$$

The period of the motion is:

$$T = \frac{2\pi}{\omega} = 2\pi\sqrt{\frac{L}{g}} \tag{C.6}$$

This means that the period and frequency depend only on the length of the string and the acceleration of gravity[54].

A pendulum makes it easier to compute the effect of acceleration on an object. In this case, our object will be the multimode fiber. The acceleration is simply:

$$a = gsin\theta, \tag{C.7}$$

where $g = 9.8m/s$, or $32ft/s$. Measuring θ and combining with g we get the acceleration applied to the fiber. We correlate those values with the speckle patterns. Of course, the periodic nature of a pendulum allows for the accumulation of sample and error statistics.

[1]When examining the series expansion for $sin\theta$, which is $sin\theta = \theta - \theta^3/3! + \cdots$. For small values of θ, we see that $sin\theta \approx \theta$. When $\theta = 15°$, the difference is about 1%.